IEEE GEOSCIENCE AND REMOTE SENSING SOCIETY SECTION

IEEE Access
Multidisciplinary ⋮ Rapid Review ⋮ Open Access Journal

Received 12 December 2025, accepted 24 December 2025, date of publication 12 January 2026, date of current version 15 January 2026.

Digital Object Identifier 10.1109/ACCESS.2026.3652346

RESEARCH ARTICLE

Assessment of Spaceborne SAR Micro-Motion Measurement for Vibration-Based SHM

ALEKSANTERI B. VATTULAINEN[1], (Member, IEEE), ALESSANDRO LOTTI[2], SEBASTIÁN DÍAZ RIOFRÍO[1], CHIARA SUPPI[2], (Graduate Student Member, IEEE), ENRICO TUBALDI[3], DANIELE ZONTA[2], PIETRO MILILLO[4,5], (Senior Member, IEEE), AND CARMINE CLEMENTE[1], (Senior Member, IEEE)

[1]Department of Electrical and Electronic Engineering, University of Strathclyde, G1 1XW Glasgow, U.K.
[2]Department of Civil, Environmental and Mechanical Engineering, University of Trento, 38123 Trento, Italy
[3]Department of Civil and Environmental Engineering, University of Strathclyde, G1 1XJ Glasgow, U.K.
[4]Cullen College of Engineering, Department of Civil and Environmental Engineering, University of Houston, Houston, TX 77004, USA
[5]Microwaves and Radar Institute, German Aerospace Center (DLR), 82234 Weßling, Germany

Corresponding author: Aleksanteri B. Vattulainen (aleksanteri.vattulainen@strath.ac.uk)

This work was supported in part by the European Space Agency under the Projects "Bridge Monitoring Based on Single Pass Synthetic Aperture Radar (SAR) Images" and "EO4Security–Innovative SAR Processing Methodologies For Security Applications-Topic B2: Micro-Doppler Processing"; in part by the ReLUIS Interuniversity Consortium "Monitoring and satellite data" under Agreement DPC-ReLUIS 2020-2022 and Agreement DPC-ReLUIS 2024-2026 WP 6; and in part by European Union–Next Generation EU, Mission 4 Component 2 under Grant CUP E53D23003560006. The work of Pietro Milillo was supported in part by the University of Houston under a contract with the National Aeronautics and Space Administration (NASA) Commercial Smallsat Data Scientific Analysis Program under Grant NNH22ZDA001N-CSDSA, in part by the NASA Commercial Smallsat Data Acquisition New Vendor Onramp Evaluation under Grant NNH23ZDA001N-CNVOE, and in part by the NASA Commercial Satellite Data Earth Science Research and Applications program under Grant NNH24ZDA001N-CESRA.

ABSTRACT Remote sensing methods for vibration-based structural health monitoring (VBSHM) are gaining interest given the benefits of non-contact sensing for this application: broader spatial coverage, easier measurement access to structures such as bridges, and cost savings from reducing the need for embedded sensor networks. Vibration measurement using micro-Doppler synthetic aperture radar (MDSAR) is an emerging technique enabling the measurement of structural vibrations from synthetic aperture radar (SAR) satellite data, exploiting recent advancements in high-resolution X-band radar imaging. This paper presents a detailed metrological assessment of MDSAR – using processing based on the pre-existing subpixel offset tracking (SPOT) concept as a representative method – to evaluate its applicability to VBSHM. Measurements are made from real SAR images of vibrating targets with synchronous ground truth data. The results verify that the technique can be used to measure target motion time-histories with dynamics relevant to SHM, namely different modulations with frequencies from 1 to 4 Hz, and radial RMS displacement amplitudes from 10.43 to 0.10 mm. These results pave the way for future measurements of infrastructure.

INDEX TERMS Frequency detection, micro-Doppler, micro-motion, SAR, vibration-based SHM, vibration measurement.

I. INTRODUCTION

Vibrometry is a popular method for structural health monitoring (SHM) due to its relative ease of implementation and potential effectiveness in identifying damage, usually achieved by observing changes in the modal parameters of a structure over time [1], [2]. Conventionally, accelerometers are used for vibration-based SHM (VBSHM). As these are contact sensors, they must be installed on the structure, where this can pose challenges in terms of hazardous working conditions and access – particularly in the case of bridges supporting arterial road or rail networks. Additionally, each sensor can only measure at a single fixed location, meaning that large structures typically require a network for adequate coverage [3]. All of these factors inflate costs and thus diminish the effectiveness of this method [4].

The associate editor coordinating the review of this manuscript and approving it for publication was Gerardo Di Martino.

A. REMOTE SENSING ALTERNATIVES

Due to the issues mentioned above, the development of remote sensing alternatives has been of interest for some time. Approaches include motion-tracking cameras using digital image correlation [5], [6] or LiDAR [7], [8], although other issues are associated with these methods: motion-tracking with cameras has the lowest measurement precision [9], is reliant on ambient lighting conditions, and along with LiDAR is sensitive to weather occlusion. Ground-based Doppler radar [10], [11], [12] solves these problems, however both LiDAR and radar sensors are very expensive, and are vulnerable to sensor movement caused by environmental conditions such as wind buffeting. If viable, passive Doppler radar making use of increasingly ubiquitous higher frequency communication signals such as 5G could help reduce costs [13], however these methods all suffer from being ground-based – requiring that they are *on-site* to make measurements – thus drastically reducing their coverage and increasing cost per monitored area.

Spaceborne sensing, such as synthetic aperture radar (SAR), presents an alternative paradigm. Interferometric SAR (InSAR) is an established technology being explored for SHM [14], [15], [16], [17], [18] and can cover very large areas (typically many kilometres), with interferometric techniques being used to measure changes in surface height. InSAR works by comparing the changes in signal phase between pixels in two registered SAR images collected at different times, which correspond to small changes in distance to the sensor at those positions. Although capable of measuring minute displacements, only very slow bulk movements can be measured as the images being compared are typically acquired days apart (if not longer) and so these techniques are not suitable for vibrometric studies.

This work instead investigates using micro-Doppler SAR (MDSAR) acting on single-pass (i.e. single acquisition) data which can observe target dynamics within the SAR acquisition time, with frequencies relevant for vibrometric SHM.

B. MOTIVATION FOR SAR VIBROMETRY

Like ground-based Doppler radar and LiDAR, SAR is a good candidate sensor for VBSHM given its sensitivity to the small changes in signal phase caused by moving targets via the Doppler effect [19]. SAR also offers the greatest possible spatial coverage of remote sensing techniques and an increasingly convenient level of temporal coverage – with highly predictable repeat passes of any area of interest – as commercial satellite constellations continue to grow. These companies include Umbra [20], Capella Space [21], and ICEYE [22], which have the capability to provide very high-resolution X-band (wavelength of $\lambda = 2.4$ to 3.8 cm) SAR images, with long dwell times/long acquisition times (t_a) – which enable MDSAR processing. Being spaceborne, these sensors are not subject to any local vibration of the sensor, unlike ground-based methods. Additionally, MDSAR techniques could assess any non-networked structure of interest much faster than conventional methods, which would expedite interventions or inspections after natural disasters – presenting a significant advantage in time critical scenarios.

The purpose of this work is thus to carry out a metrological assessment of an MDSAR technique via experimental tests, where ground truth data were synchronised with satellite acquisitions. Whilst several MDSAR measurement techniques have been published, none have been comprehensively evaluated in this way previously. In this work, the sub-pixel offset tracking (SPOT) method is used to make vibration measurements from SAR data as a representative technique. Data of an isolated, high reflectivity target were collected with the target undergoing motion with a range of frequencies, amplitudes, and modulations. The majority of tests involved very low amplitudes relevant to SHM use cases, where the scope of the work is defined as an evaluation of the potential and limitations of MDSAR techniques for VBSHM.

C. STATEMENT OF NOVELTY

The key novelty of this work is the metrological evaluation of MDSAR measurements of motion typical of civil infrastructure. It quantifies the capabilities and limitations of the SPOT method across a range of realistic scenarios, to the lowest verified amplitude and velocity motions to date. Another important novelty is the reconstruction of the full-time histories of target vibrations (including both frequency and amplitude) validated through synchronised ground truth measurements acquired during the spaceborne SAR data acquisitions, these having previously been demonstrated only in a very limited capacity [23], [24]. This assessment provides robust evidence that this information is captured in SAR data, and that this can already be recovered with relatively simple signal processing techniques such as SPOT.

Following the introduction in Section I, Section II covers the basics of SAR as needed to interpret the results and provides a brief overview of SAR micro-motion measurement methods. Section III then explains the MDSAR processing method used in this work. Section IV details the SAR and ground truth data collection, followed by the results of the study in Section V. The paper then ends with Sections VI and VII with the discussion and conclusions.

II. SAR BACKGROUND

SAR is a radar imaging technique which exploits sensor movement to improve image azimuth resolution. During the data acquisition period, the SAR (mounted on a satellite) receives echoes of reflected pulses from the scene whilst moving some distance along its orbit. By recording information about the position and velocity of the SAR during acquisition, the phase changes these induce in the received signal can be compensated for, and the data from the full acquisition focused to form an image. By doing this, the section of the orbit covered during the acquisition is in effect *synthesised* to become the sensor antenna. The synthetic aperture greatly improves the image azimuth resolution (since

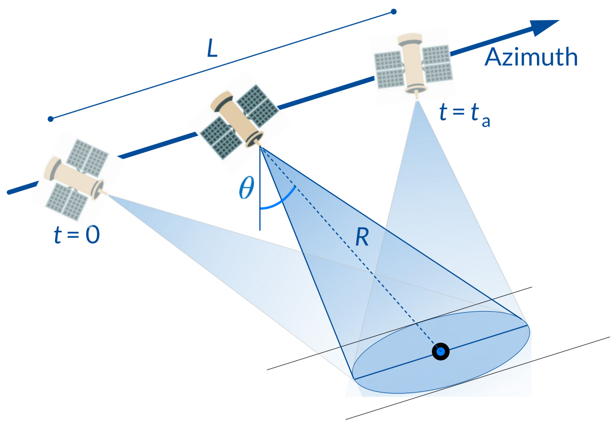

FIGURE 1. **SAR imaging geometry for a spotlight mode acquisition. The diagram illustrates the squinting behaviour of the sensor whereby it changes the antenna pointing angle during the acquisition. Key features shown include the satellite flight direction (labelled as azimuth), the total acquisition duration (from $t = 0$ to $t = t_a$), the synthetic aperture length (L), the slant range (line of sight, LOS) distance ($R(t)$), and the incidence angle (θ).**

this is inversely proportional to the aperture length) far beyond what is possible with the real aperture antenna on board [25].

The image azimuth direction is defined as parallel to the SAR movement, whereas range is perpendicular, as shown in the SAR imaging geometry diagram in Fig. 1, which shows a 'spotlight' mode acquisition. Several SAR imaging modes exist, however this study considers spotlight mode acquisitions due to the greater target observation time this provides.[1] In spotlight mode, the beam angle of the SAR antenna ('squint angle') is steered such that the centre of the target area remains illuminated as the platform moves (as shown in Fig. 1) for the entire observation time. The achievable azimuth resolution, Δx, is given in Eq. 1:

$$\Delta x = \frac{\lambda \cdot R(t)}{2 \cdot v_p \cdot t_a} \tag{1}$$

where λ is the centre wavelength of the transmitted signal and v_p is the platform (satellite) velocity.[2]

Figure 1 also shows the definitions of the incidence angle, θ, the slant (also known as line of sight, LOS) range $R(t)$, and the *synthetic aperture* length L travelled by the platform over the acquisition time from $t = 0$ to $t = t_a$.

An example of a SAR image formed from spotlight mode data is shown in Fig. 2, showing some basic phenomenology. The image grid has the axes of azimuth and (slant) range, where these are often simply given as pixel number but can be scaled to distances. Figure 2 is produced from a common SAR image product known as sensor independent complex data (SICD) [26] which provides pixel intensity (reflectivity) and phase information. Complex data are necessary for the processing method described in this paper, where it must also be 'single-look complex' (SLC) data as opposed to 'multi-look complex' (MLC) data, as in the former only one continuous observation is used to form the image rather than the multiple integrated images in the latter. The use of multiple image acquisitions causes temporal averaging that corrupts any motion information in the data and renders this unusable for MDSAR.

A. THE MICRO-DOPPLER EFFECT IN SAR

Numerous SAR image formation processes exist, however typically they assume that the observed scene is stationary when performing the signal phase compensation methods that focus the image. Moving targets thus have uncompensated signal phase (due to the Doppler effect), which results in target displacements, distortions, or artefacts in the final image [19]. For example, a target moving with constant velocity will appear offset and smeared (defocused) along the azimuth direction in the SAR image. An example of these effects is shown in Fig. 3, which shows a moving ship displaced from its wake at sea due to the radial velocity component of the ship relative to the SAR observation. In the case of a strongly vibrating target, this results in the appearance of several 'paired echoes' centered around the true position of the target [27], [28], as seen in Fig. 5(a), for example.

The phase changes induced by the Doppler effect are caused by radial velocities, thus the radar can only observe motion in the LOS direction. Due to the one-to-one mapping of Doppler shift bins to azimuth bins in SAR imaging, the radial velocities manifest as artefacts predominantly in the azimuth direction rather than range [29]. This relationship is shown in Eq. 2:

$$x(t) = -\frac{v_r \cdot R(t)}{v_p} \tag{2}$$

where $x(t)$ is the offset distance along the azimuth direction, and v_r is the radial velocity (along the LOS) of the target relative to the moving SAR sensor.

In the field of radar, the changing Doppler frequency shift observed from targets which are oscillating or vibrating (or in general undergoing some periodic or secondary motion) is known as *micro-Doppler*, and arises from the *micro-motion* (m-m) of the target. Vibrometric measurements with SAR (and radar more broadly) thus fall into the field of micro-Doppler measurement and phenomenology. To achieve the measurement of micro-Doppler, sampling of the signal as a function of time is required. The SLC SAR image product has no temporal resolution since it is formed from the integrated data from the whole aperture, however if the data is segmented to form *sub-aperture* images (where each image is formed from a smaller section of the full acquisition), time resolution can be achieved. This concept is

---

[1] The mathematical concepts and algorithms shown in this work also apply to other image acquisition modes such as Stripmap, however the effectiveness of MDSAR in other modes is more limited due to the shorter achievable observation times.

[2] This formula is derived from the formula for the azimuth resolution of spotlight mode SAR, $\Delta x = \frac{\lambda}{2\phi}$, applying the small angle approximation for the subtended angle of the aperture, ϕ.

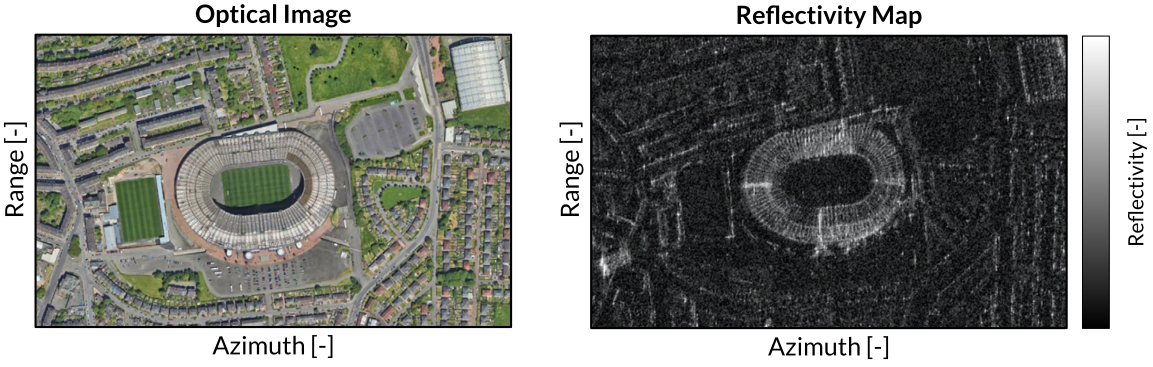

(a) (b)

FIGURE 2. **(a) Optical image, and (b) reflectivity map from a spotlight acquisition over Hampden Park Stadium in Glasgow, captured by the Umbra-04 sensor on the 14th of March 2024 at 20:35:48 (UTC).**

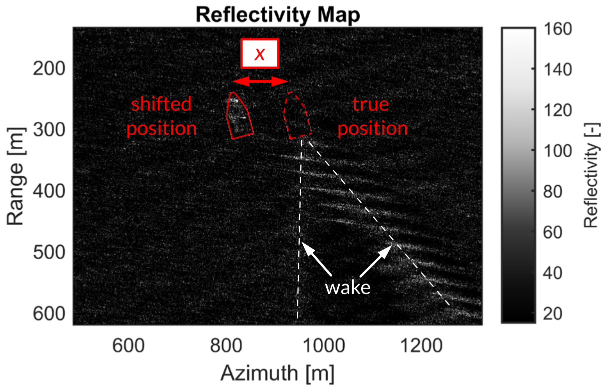

FIGURE 3. **Example of the effects of a constant velocity target on SAR imaging. The figure shows the shifted position of a moving ship in the reflectivity map of a SAR image, captured by the Capella-10 sensor on the 5th of February 2025 at 11:49:46 (UTC).**

illustrated in Fig. 4. Segmenting the data comes at the cost of coarser azimuth resolution in the resultant images as dictated by Eq. 1, however this issue can be mitigated with the use of overlapping sub-aperture windows or by longer full aperture lengths such as those afforded by spotlight mode acquisitions.

B. MICRO-DOPPLER MEASUREMENT FROM SAR

Several different methods have been devised for the measurement of m-m from SAR data, and are discussed below as a small number of broad algorithm classes. For a deeper review, the reader is invited to refer to Rollo et al. [28].

1) TIME-FREQUENCY ANALYSIS

These methods involve the use of different transforms to estimate the Doppler frequency in a given time window, producing measurements of target motion over time. Long windows are often used to maintain sufficient frequency (and thus velocity) resolution, where these are then significantly overlapped to mitigate loss of time resolution. The most frequently used transform for this kind of processing is the short-time Fourier transform (STFT), generating the commonly known spectrogram. Many other transforms have been used for micro-Doppler analysis more broadly, with examples tabulated in Chen et al. [30] such as the Wigner-Ville distribution (WVD). The work by Chen et al. used time-frequency analysis to measure a vibrating corner reflector from SAR data with the reasonable accuracy of 2.3 Hz versus a ground truth value of 2.0 Hz, however the results were presented without additional amplitude verification. Rüegg et al. [27] used the smoothed pseudo-WVD and the Gabor transform to analyse vibrating and rotating targets in SAR images, where the changing Doppler frequency of a corner reflector rotating at 1 Hz was observed.

More recently, a modified back-projection approach was used as a new way to construct the signal of interest. This method has been used to measure a vibrating corner reflector with a frequency of 2.00 Hz and an amplitude of 15 mm, returning an accurate frequency estimate using a time-frequency method presented in Clemente et al. [23]. Similar time-frequency methods applied to back-projected data of a bridge in Glasgow yielded estimated vibrational spectra showing several modes of interest matching synchronous ground truth data collected using accelerometers. Whilst the technique correctly identified many vibrational modes, the relative amplitudes were not a match due to the limitations of the approach [31], although this work presents the first synchronous measurements of structural vibrations with conventional (accelerometer) sensors and SAR, to the authors' knowledge.

2) PHASE DOMAIN

The second broad class of methods measure the changing signal phase directly. These include the discrete fractional Fourier transform (DFrFT), which is an extension of the discrete Fourier transform (DFT) which can be used to estimate rates of frequency change. This was used in papers by Wang et al. [32], [33] in efforts to suppress paired echo artefacts in SAR images. Experimental data of vibrating corner reflector targets were presented with good results in

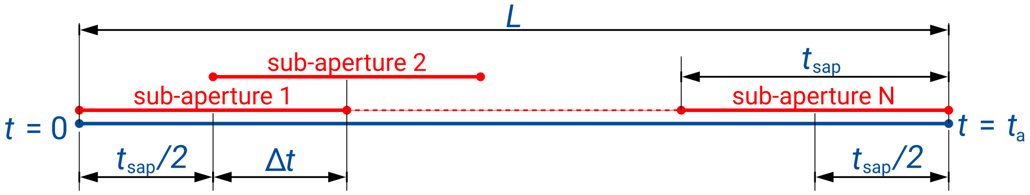

FIGURE 4. Diagram showing the segmentation of a synthetic aperture of length L, duration t_a, into N overlapping sub-apertures of duration t_{sap}, separated by the time resolution, Δt.

two scenarios, the first with settings of 1 Hz frequency and 1.5 cm amplitude, and the second with 5 Hz frequency and 1.5 mm amplitude. Amplitude estimates from the measurements were not reported, however the frequency accuracy of the results were good: 0.9 Hz was measured for the former experiment, and 5.2 Hz for the latter [32].

Another example of a phase signal estimator is the high-order ambiguity function (HAF). This works by assuming the phase can be modelled as a polynomial phase function (PPS), and then iteratively estimating the coefficients of the PPS in each time window. This method has been applied in an SHM context, measuring movements of the PuyLaurent Dam in France. In this experiment the m-m of a corner reflector placed at the ridge of the dam was measured, producing vibrational frequency results which are consistent with previously reported in situ values, however without any simultaneous measurement or comparison of amplitude [34]. A recent approach which has been investigated involved measuring the Doppler centroid of targets over a sequence of sub-aperture images to estimate displacements over time. This was used on data of a water tower and a bridge in the Basilicata region of Italy, and compared favourably with asynchronous measurements by a ground-based radar [35].

Other approaches include the use of a quasi-maximum likelihood estimator to track the signal phase, showing promising results on simulated data and being remarkable as an example of a statistical approach [36].

The same modified back-projection approach as presented in Clemente et al. [23] above was initially pursued to allow the phase to be directly measured over time. A direct extraction of the signal phase from the back-projected data in Rollo et al. [24] yielded promising results of a frequency estimate of 2.01 Hz and amplitude of approximately 16 mm, however phase unwrapping errors and vulnerability to clutter remain an obstacle to this approach.

3) IMAGE DOMAIN

The final class of SAR m-m measurement algorithms are those operating in the image domain, often known as pixel tracking methods. Clemente et al. [23] used a simple approach to measure the motion of a corner reflector with a nominal frequency of 2 Hz and 15 mm amplitude, where the position of the target intensity maximum was tracked over a sequence of sub-aperture image frames. This accurately estimated the frequency, and yielded an amplitude estimate of approximately 18 mm, and prior to this work was the only pixel tracking result with simultaneous ground truth verification.

The aforementioned SPOT method used in this work also belongs to this class, where for this technique 2D cross-correlation is used for image registration between each sub-aperture image to detect the apparent shift of the target due to the Doppler effect. The term ‘sub-pixel’ refers to the upsampling of the sub-aperture images which is used to increase the precision of the shift estimates. This method has been demonstrated for SHM using case studies of several bridges in Italy in Biondi et al. [37], where crack localisation matching photographs is shown, however without ground truth verification of vibrational dynamics with conventional sensing. A case study of the destabilisation of the Mosul Dam in Iraq has also been published [38], where some cracks identified with SPOT coincide with those identified using interferometric SAR (InSAR) [39], these being very similar to damage identified by in situ measurements.

SPOT has in general shown many promising results in applications involving SHM and is likely the most established method for measuring m-m from SAR, having been applied to the most use cases and experimental data. The results presented in the literature have however lacked verification with synchronous ground truth measurements, where the results presented in this work aim to begin to fill this gap and improve the rigour of future measurements.

III. SPOT METHOD

This section outlines the method for estimating the vibrational velocities of ground targets from single-pass SAR images using the SPOT technique. This implementation of the SPOT algorithm is inspired by similar pixel-tracking methods [37], [38].

A. SUB-APERTURE GENERATION

The processing begins with the generation of the azimuth sub-aperture sequence from the full acquisition data, taking as input a SAR SLC image. To reduce computational load, the SAR image is cropped around the target by defining a region of interest (ROI). A 1D Fast Fourier Transform (FFT) is then applied to the ROI along the azimuth dimension to convert the data from the range-azimuth domain to the ‘range-azimuth frequency’ domain. The data for the sequence of N sub-apertures are then segmented from this by applying a series

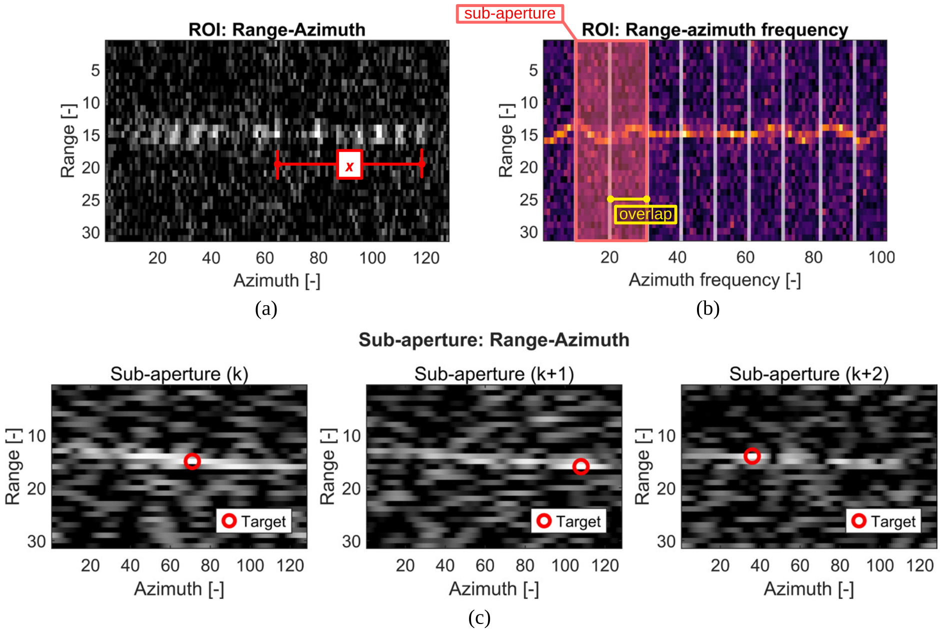

(a) (b) (c)

FIGURE 5. **(a) ROI reflectivity image in range-azimuth coordinates, showing the azimuth displacement, x, of a vibrating ground target; (b) the range-azimuth frequency plot generated from the ROI using an FFT in the azimuth dimension, where the segmentation of this data into sub-apertures is determined by the sub-aperture fraction, α, and the overlap, Ω; and (c) examples of sub-apertures in range-azimuth coordinates indicating pixel tracking.**

of N bandpass filters, where each is centred at increasing azimuth frequencies. The proportion of the full acquisition data (or bandwidth) used for each sub-aperture is described by the aperture fraction, α, defined as:

$$\alpha := \frac{t_{\mathrm{sap}}}{t_{\mathrm{a}}} \tag{3}$$

where t_{sap} is the sub-aperture duration. This is the observation window of the instantaneous vibrational motion, where to facilitate comparison of processing parameters when observing vibrations with different periods, T, the observation ratio, η, is defined:

$$\eta := \frac{t_{\mathrm{sap}}}{T} \tag{4}$$

where T is the period of the highest frequency component.

Similar to time-frequency analysis techniques such as the spectrogram, the windows used to segment the sub-aperture data can overlap to improve temporal resolution whilst maintaining a large aperture fraction, which corresponds to a better azimuth resolution by Eq. 1. In common with the general method for computing overlapping windows, the degree of overlap is parameterised by the overlap ratio Ω. The number of sub-apertures corresponding to the specified values of α and Ω is then computed using Eq. 5.

$$N = \frac{t_{\mathrm{a}} - \Omega \cdot t_{\mathrm{sap}}}{t_{\mathrm{sap}} - \Omega \cdot t_{\mathrm{sap}}} = \frac{\alpha^{-1} - \Omega}{1 - \Omega} \tag{5}$$

The segmented data are then transformed back into the range-azimuth domain using an inverse FFT (IFFT). Prior to this step, the segmented data are zero-padded to be of the same dimension as the input ROI, such that the pixel spacing of each sub-aperture image is the same as the original. The sub-aperture generation processing is summarised in Fig. 5.

B. MOTION TRACKING

As shown in Eq. 2, due to the instantaneous radial velocity v_{r} of the target at each time step, the target is observed as shifted by varying amounts in azimuth in each sub-aperture. This shift is tracked by identifying and following the azimuth position, x, of a bright pixel across the sequence of sub-apertures using 2D cross-correlation. The cross-correlation registers a reference and a test image patch, with each having matching azimuth and range widths (w_x and w_y, respectively) in terms of pixels. The reference patch is selected from the middle sub-aperture frame, with each test patch selected in sequence beginning from the first frame. During the registration process, the patches are further upsampled by a factor A to measure shifts with sub-pixel precision. Finally, the series of azimuth pixel displacements is then converted into a radial velocity time history using Eq. 2.

The time axis of the reconstructed velocity signal is generated in the same way as for a spectrogram. Each velocity value is associated with the centre of its respective sub-aperture window. As such, the time axis is defined as a linearly spaced vector of N values, ranging from $t_{\mathrm{sap}}/2$ to $t_{\mathrm{a}} - t_{\mathrm{sap}}/2$, as shown in Fig. 4. This results in a temporal

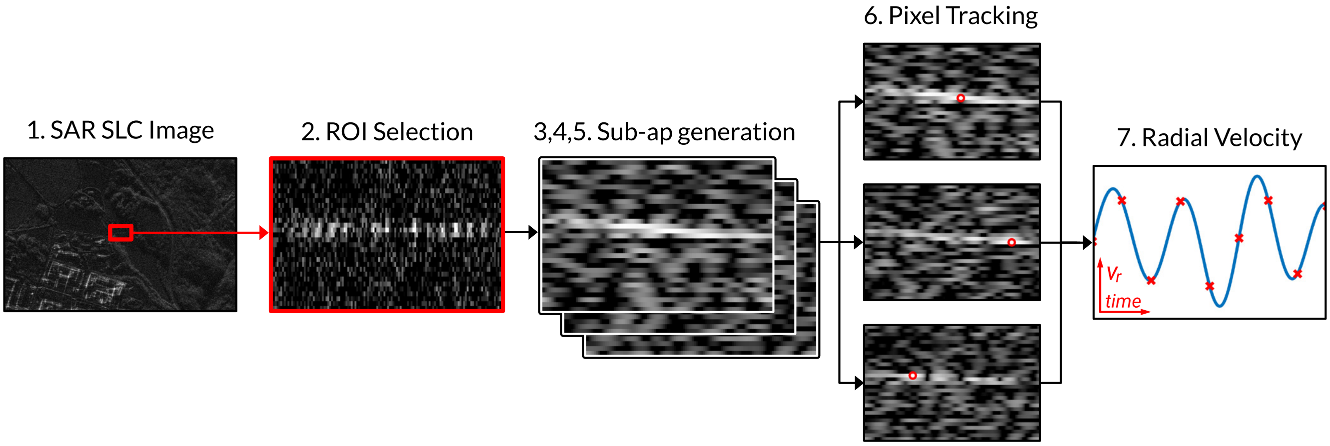

FIGURE 6. Diagram illustrating the SPOT algorithm workflow.

resolution (i.e. sampling period) as shown in Eq. 6:

$$\Delta t = \frac{t_a - t_{sap}}{N - 1} \tag{6}$$

where the sampling frequency, f_s, is given by $1/\Delta t$. Since this method uses only a single acquisition, it can only resolve motion which has a maximal period on the scale of the observation time, t_a.

To enhance the temporal resolution of the SAR measured velocity signal, Whittaker–Shannon interpolation (better known as sinc interpolation) is applied. This technique allows for the reconstruction of a continuous-time signal from its discrete samples, under the assumption that the signal is band-limited [40]. In this work, sinc interpolation was used to upsample the coarse SAR measured velocity signal by a factor B, improving the extracted amplitude estimates while preserving the original frequency content.

The fundamental steps of the SPOT algorithm are summarised below:

1) Begin with the full SLC SAR image.
2) Crop the data to the ROI around the target.
3) Apply an FFT along the azimuth dimension of the ROI.
4) Segment the data into N sub-apertures, where N is given by Eq. 5 based on the chosen aperture fraction α and overlap ratio Ω.
5) Zero-pad and apply an IFFT to each segment of the data to reconstruct a series of sub-aperture images in range-azimuth with the same pixel spacing as the ROI.
6) Select the brightest pixel within the scene on which to centre a patch of $w_x \cdot w_y$, and track the motion of this patch through the sequence of sub-aperture frames using 2D cross-correlation, using an upsampling factor A.
7) Convert pixel shifts into radial velocity values using Eq. 2 and apply sinc interpolation with an upsampling factor B.

Figure 6 graphically illustrates the overall SPOT algorithm workflow. Steps 3, 4, and 5, which correspond to the sub-aperture generation process, are further detailed in Fig. 5.

IV. EXPERIMENTAL DATA AND GROUND TRUTH COMPARISON

This section describes the experiments conducted to test the SPOT algorithm. The collection of the ground truth data is described first, followed by a description of the SAR data. Finally, the processing of the ground truth data and the subsequent analysis comparing the SAR measurements and ground truth values is explained.

A. GROUND TRUTH DATA

1) EXPERIMENT LOCATIONS

To ensure a controlled environment and reduce potential sources of interference, the vibrating targets used in the experiments were placed in open grassy areas far from other reflective objects such as large buildings or metal structures. The tests were conducted at two locations: Villa Gherta in Trento, Italy, and Glasgow Green, Glasgow, Scotland. These locations are shown in Fig. 7.

2) INSTRUMENTATION

The vibrating 'shaker' targets were set up by mounting a corner reflector (CR) target on a linear actuator. CRs are commonly used in radar measurements to provide a point-like high intensity reflection which is stable over a wide angle [43]. The shaker in Glasgow used a TIRA-TV 51140 [44] whilst in Trento this was an APS-400 [45]. Photographs of the apparatus in situ are shown in Fig. 8(a)-(b). Both configurations produced only vertical motion to simplify the validation process, which was controlled using a signal generator input. A diagram of the SAR collection geometry in relation to the shaker movement is also shown in Fig. 8(c). The vertical displacements produced by the

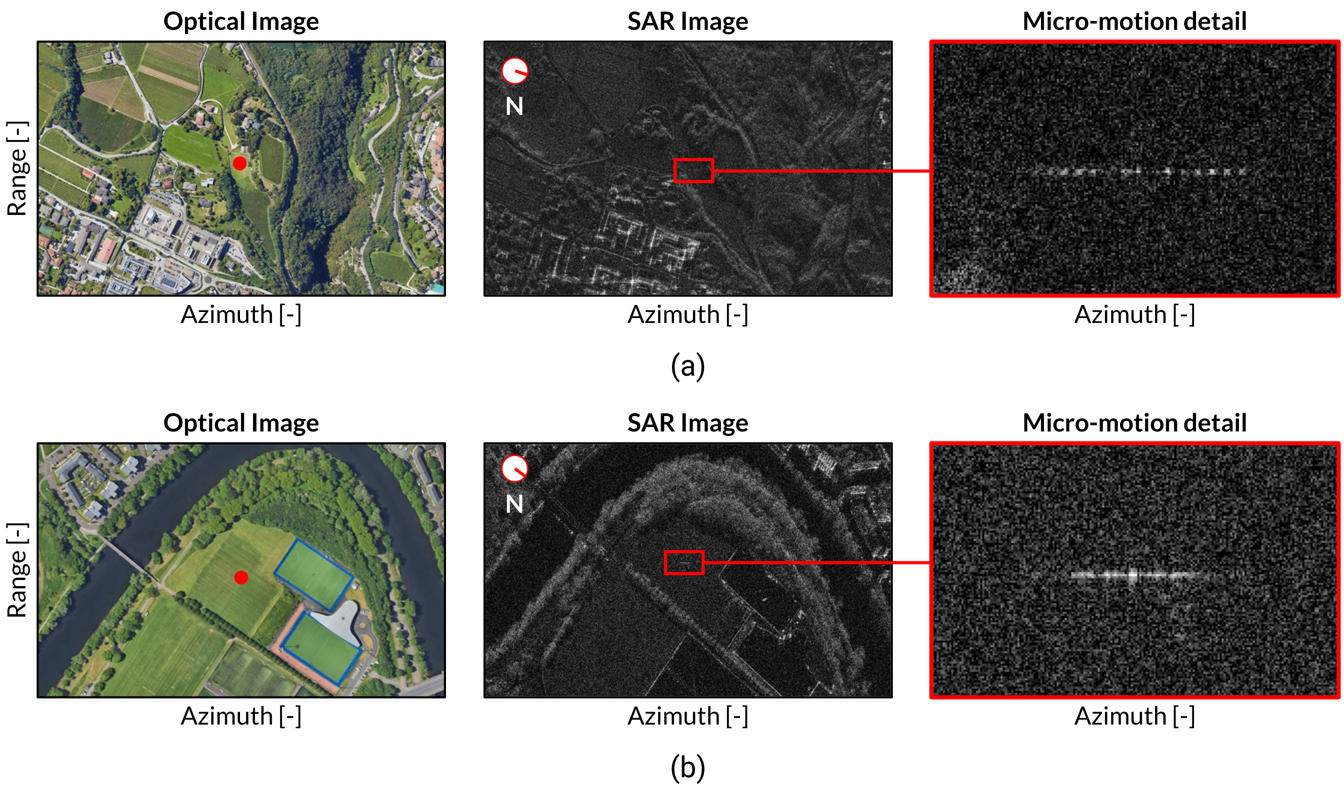

FIGURE 7. The test locations shown as both optical and SAR images, with detail of micro-motion seen from a shaker target in (a) Villa Gherta in Trento LAT: 46.06814°, LON:11.14684°; and (b) Glasgow Green in Glasgow LAT: 55.84379°, LON:−4.23634°.

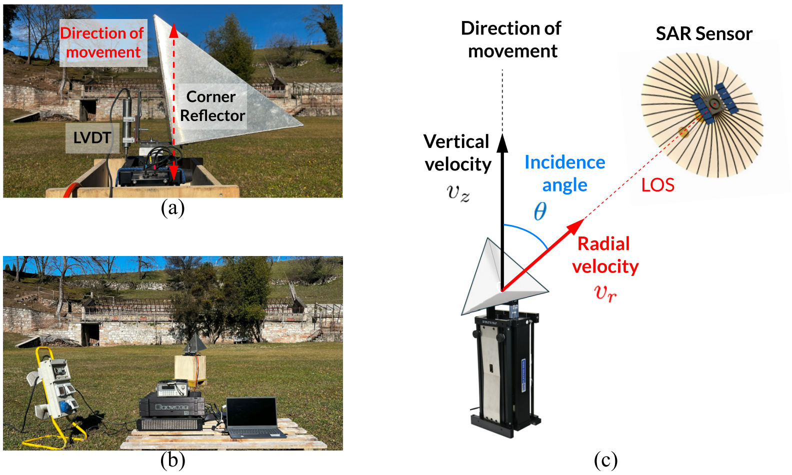

FIGURE 8. Photographs in (a) and (b) show the experimental apparatus in situ at the Villa Gherta site, including the actuator, CR, LVDT, and data acquisition system, and (c) shows a diagram of the SAR acquisition geometry in relation to the shaker setup. Images adapted from [41] and [42].

apparatus were recorded using a linear variable differential transformer (LVDT) sensor.

3) PROCEDURE

First, the CR was tilted 20° vertically and then oriented in azimuth to face towards the direction of the satellite during its passage, taken as the opposing angle to the mean azimuth angle of the acquisition. The instrumentation described above was then activated 10 minutes prior to the start of the scheduled satellite observation time (which has a degree of uncertainty) to ensure that coincident data were collected and that the shaker motion had settled to a steady state. Data collection continued for a further 10 minutes after the scheduled time, during which the

LVDT sampled the displacement of the CR at a sampling rate of 50 Hz. The programme of tests involved motions with various amplitudes, frequencies, and modulations to comprehensively test the algorithm under different conditions in preparation for more complex case studies involving real structures.

The resultant tests included a variety of vibration signals, ranging from single tone sinusoids to more complex signals such as a linear frequency sweep, a superposition of multiple frequencies, and a number of amplitude-modulated (AM) signals with either a 1 or 2 Hz carrier frequency with a 0.2 Hz modulation. These signal types were selected to evaluate SPOT across a range of vibrational scenarios relevant to SHM. Single tone signals reflect typical structural responses near fundamental modes, while amplitude-modulated signals mimic responses from multiple closely-spaced modes (e.g. typically observed in long-span bridges and viaducts). Frequency-varying signals, although less common in SHM, allow the assessment of the technique under more complex conditions that could be useful in other contexts. The SAR measures only the LOS projection of the target motion. For the sake of experimental simplicity, the shakers move only vertically. To disambiguate motion components along multiple axes, two or more measurements from different perspectives are needed, however for bridges the dominant direction of motion is vertical – this case matches the experiments well and can be measured with only a single observation given this prior knowledge.

In this study, 9 different configurations were tested, with the resulting peak radial displacement, $d_{\mathrm{r,max}}$, of the shaker being as large as 13.96 mm with a peak radial velocity, $v_{r,\mathrm{max}}$, of 95.52 $\mathrm{mm\,s^{-1}}$ down to a displacement of 0.19 mm and a peak radial velocity of 1.42 $\mathrm{mm\,s^{-1}}$. The experiment configurations are listed in Table 1.

B. SAR DATA

The SAR dataset consists of 9 Umbra acquisitions corresponding to the tests described in Table 1. Umbra is a constellation of X-band SAR satellites capable of providing high-resolution data promptly for both private and public use [20]. The radar sensors operate at a central frequency of 9.6 GHz, corresponding to a wavelength of $\lambda = 31$ mm. All of the acquisitions were collected using the Umbra spotlight high-resolution mode. The main acquisition parameters of the SAR images are reported in Table 2, including the SAR sensor satellite used for the acquisition, date and time of the acquisition, duration of the acquisition t_{a}, collection incidence angle θ, pulse repetition frequency (PRF), SAR platform velocity v_{p}, slant range distance R, range resolution Δy, and azimuth resolution Δx.

C. GROUND TRUTH COMPARISON

1) PROCESSING OF GROUND TRUTH

The ground truth data were processed to LOS velocities and synchronised with the acquisition to provide a meaningful comparison with the SAR measurements. This processing involved:

1) **Numerical derivation**: the recorded vertical displacement data were differentiated to obtain vertical velocity values.
2) **Time cropping**: the velocity time history was cropped to match the satellite acquisition window by centring this on the centre of aperture time t_{COA}.
3) **Satellite geometry computation**: the satellite geometry during the acquisition was calculated to determine the LOS angle at each point in the time history.
4) **Velocity projection**: the vertical velocity was projected onto the radial direction (LOS) of the satellite using the incidence angle θ [°] to compute the radial velocity v_r. This projection is shown in Fig. 8.

2) COMPARISON METRICS

The following metrics were chosen to evaluate the quality of the SAR measurement with respect to the ground truth data, in both the time and frequency domains, for each individual test:

- RMSE: root mean square of the error (RMSE) between the two signals computed in the time domain by comparing the SAR and ground truth measured velocities at corresponding time instants,
- ϵ_f: absolute error between the dominant frequency peaks,
- ρ_t: Pearson's coefficient for correlation in the time domain,
- ρ_f: Pearson's coefficient for correlation in the frequency domain.

As discussed above, the SAR and ground truth time series were aligned using t_{COA}, however a small uncertainty in the synchronisation remained. To account for this, the SAR signal was allowed to shift within a time interval of half the period [-$T/2$, $T/2$] of the lowest frequency component to maximise the time-domain correlation ρ_t between the two signals. This was assumed to minimise the synchronisation error, and the same time shift was then applied when calculating the RMSE. To optimise the processing settings of sub-aperture duration, overlap ratio, and patch size, a parameter sweep was performed and the results selected based on maximising the temporal correlation with the corresponding ground truth.

V. RESULTS

In this section, the results of the SPOT technique are presented with comparison to the ground truth data. Each SAR acquisition was processed following the workflow described in Section III, with Table 3 summarising the parameters used for each extraction and the resulting metric outputs. The presentation of results is structured into three parts according to signal type: single tone, AM, and superposition and frequency sweep.

The processing parameters listed in Table 3 include:

TABLE 1. The configuration of the conducted tests, noting the test number, type of signal, the principal frequencies (f), the peak ($d_{z,\max}$) and RMS ($d_{z,\mathrm{RMS}}$) values of the vertical displacement, the peak ($v_{z,\max}$) and RMS ($v_{z,\mathrm{RMS}}$) values of the vertical velocity, the peak ($d_{r,\max}$) and RMS ($d_{r,\mathrm{RMS}}$) radial displacements, and the peak ($v_{r,\max}$) and RMS ($v_{r,\mathrm{RMS}}$) values of the radial velocity of the oscillations.

Test	Signal	f	$d_{z,\max}$	$d_{z,\mathrm{RMS}}$	$v_{z,\max}$	$v_{z,\mathrm{RMS}}$	$d_{r,\max}$	$d_{r,\mathrm{RMS}}$	$v_{r,\max}$	$v_{r,\mathrm{RMS}}$
–	–	[Hz]	[mm]	[mm]	[mm s^{-1}]	[mm s^{-1}]	[mm]	[mm]	[mm s^{-1}]	[mm s^{-1}]
1	Single tone	1	24.10	17.42	165.86	111.24	13.96	10.43	95.52	64.11
2	Single tone	2	3.43	2.53	48.26	31.79	2.24	1.65	31.38	20.70
3	Single tone	2	1.08	0.80	16.55	10.24	0.70	0.52	10.75	6.66
4	AM	2 (0.2)	0.52	0.26	7.12	3.17	0.39	0.19	5.25	2.34
5	AM	2 (0.2)	0.29	0.14	4.34	1.77	0.22	0.10	3.21	1.31
6	AM	1 (0.2)	0.53	0.28	3.83	1.78	0.43	0.23	3.13	1.46
7	AM	1 (0.2)	0.24	0.13	1.74	0.81	0.19	0.10	1.42	0.66
8	Superposition	2 and 4	2.60	1.56	51.63	29.27	1.11	0.66	21.99	12.47
9	Frequency sweep	1 to 4	4.03	2.81	84.33	38.47	2.81	1.98	58.04	26.53

TABLE 2. SAR acquisition parameters: test number, sensor name, acquisition date, time at the start of the acquisition in UTC, observation time (t_a), incidence angle (θ), pulse repetition frequency (PRF), satellite velocity (v_p), slant range distance (R), range resolution (Δy), and azimuth resolution (Δx).

Test	Sensor	Date	Time (UTC)	t_a	θ	PRF	v_p	R	Δy	Δx
–	–	[dd-mm-yy]	[HH:MM:SS]	[s]	[°]	[kHz]	[km s^{-1}]	[km]	[m]	[m]
1	Umbra05	18/11/23	20:46:27	6.04	54.80	5.75	7.69	844	0.18	0.22
2	Umbra04	14/03/24	20:35:48	5.41	49.36	6.37	7.70	716	0.17	0.22
3	Umbra05	14/03/24	21:29:22	5.95	49.43	6.31	7.67	795	0.17	0.21
4	Umbra09	24/02/25	10:53:09	16.01	42.29	7.44	7.65	749	0.15	0.08
5	Umbra10	25/02/25	10:52:49	15.93	42.00	6.92	7.65	745	0.15	0.08
6	Umbra09	30/01/25	10:46:27	14.70	34.49	7.75	7.65	683	0.13	0.07
7	Umbra09	31/01/25	10:46:52	14.79	35.05	7.71	7.65	687	0.13	0.07
8	Umbra08	29/03/24	20:57:41	7.98	64.78	6.11	7.66	1115	0.20	0.22
9	Umbra04	29/03/24	21:29:38	6.38	46.29	5.44	7.70	673	0.16	0.18

- The patch size in pixels along the azimuth (w_x) and range (w_y) directions.
- The observation ratio (η), where this was computed relative to the period of the carrier frequency – for the superposition and frequency sweep signals, the period associated with the highest frequency component was used.
- The overlap ratio (Ω).
- The resulting number of sub-apertures (N).
- The sampling frequency (f_s).
- The sub-aperture duration (t_{sap}).
- The frequency resolution in the spectral domain (Δf).

Additionally, the ROI size during processing was defined as 650 range pixels by 3000 azimuth pixels, and upsampling factors of $A = 10$ and $B = 20$ were used. The performance of the SPOT algorithm was assessed both graphically with Figures 9 to 17, and numerically using the metrics outlined in Section IV-C2, with the results presented in Table 3. In the case of the RMSE, this is expressed both in terms of velocity and as a percentage of the maximum ground truth radial velocity to help facilitate comparison of the results. During the acquisition time, the range to the target observed by the SAR changes, however the image formation process fully compensates the change such that R is a constant in the image product used as input to the SPOT processing, with values as shown in Table 2.

A. SINGLE FREQUENCY

1) PROCESSING PARAMETERS

Tests 1 to 3 were of single frequency sinusoids with a frequency of either 1 Hz or 2 Hz, with maximum radial velocities ranging from $v_{r,\max} = 95.52$ to 10.75 mm s^{-1} (RMS radial values of $v_{r,\mathrm{RMS}} = 64.11$ to 6.66 mm s^{-1}), with corresponding RMS radial displacements, $d_{r,\mathrm{RMS}}$, of 10.43 mm to 0.52 mm. As summarised in Table 3, these were extracted with observation ratios η ranging from 0.39 to 0.57 corresponding to comparable t_{sap} values of 0.39 s to 0.24 s. The observation ratio used for the extraction in Test 3 exceeded 0.5 meaning that the sub-aperture duration was greater than half of the period being observed, however the overlap percentage of 38% ensured that the sampling frequency met the Nyquist criterion. In general, the overlap percentages for these tests were similar, ranging from 38% to 43%. The azimuth patch size was 131 for Test 1, after which it was decreased to 101 for Tests 2 and 3. This was found to improve tracking performance and was dependent on the target velocity, where it was observed that too small a patch size would result in the tracking underestimating the movement.

TABLE 3. SPOT extraction parameters and metric results comparing the SAR measured velocities with ground truth data. The table lists the test number, patch range size (w_y), patch azimuth size (w_x), observation time (t_a), observation ratio (η), overlap percentage (Ω), sub-aperture number (N), sampling frequency (f_s), sub-aperture duration (t_{sap}), frequency resolution (Δf), absolute and percentage RMSE, absolute error between dominant frequency peaks (ϵ_f), correlation in the time domain (ρ_t), and correlation in the frequency domain (ρ_f).

Test	w_y	w_x	t_a	η	Ω	N	f_s	t_sap	Δf	RMSE	RMSE	ϵ_f	ρ_t	ρ_f
–	[pixels]	[pixels]	[s]	–	[%]	–	[Hz]	[s]	[Hz]	[$\mathrm{mm\,s^{-1}}$]	[%]	[Hz]	–	–
1	5	131	6.04	0.39	43	26	4.4	0.39	0.18	20.6	21.6	0.0090	0.95	0.97
2	5	101	5.41	0.48	38	35	6.6	0.24	0.19	9.6	30.6	0.091	0.89	0.96
3	5	101	5.95	0.57	38	33	5.6	0.28	0.18	4.9	45.6	0.045	0.73	0.87
4	5	51	16.01	0.58	23	71	4.5	0.29	0.064	2.3	43.8	0.050	0.61	0.71
5	5	71	15.93	0.62	31	74	4.7	0.31	0.064	2.2	68.5	0.015	0.45	0.73
6	5	51	14.70	0.66	49	42	2.9	0.66	0.071	1.2	38.3	0.0010	0.68	0.75
7	5	51	14.79	0.65	42	38	2.6	0.65	0.071	0.91	64.1	0.014	0.48	0.70
8	5	71	7.98	0.66	41	81	10.2	0.17	0.13	13.9	63.2	0.083	0.51	0.67
9	5	131	6.38	0.69	45	66	10.5	0.17	0.16	11.9	20.5	0.079	0.89	0.95

2) QUALITATIVE ANALYSIS

Figures 9 to 11 show the time series and frequency spectra of the velocity measurements. These results indicate that the signals measured by SAR match the ground truth well both in the time and frequency domains. In all cases, the main vibration frequency was accurately detected, as shown by the spectrum results. The measured peak amplitude values are also satisfactory, however with a tendency to be slightly underestimated, indicating a measurement bias which is more pronounced in Tests 2 and 3. Test 2 (Fig. 10) exhibits a generally good match in the time series, however with some peaks being under- or overestimated, and with consequently a diminished spectral peak and spurious frequency components at 0.5 and 2.8 Hz. Test 3 (Fig. 11) shows similar results, confirming the overall measurement consistency although again with some minor measurement noise in the spectrum. A degradation in performance was observed as the vibration velocity decreases – in this case from 95.52 $\mathrm{mm\,s^{-1}}$ to 10.75 $\mathrm{mm\,s^{-1}}$ from Test 1 to Test 3 – which affected both the smoothness of the time series and the sharpness of the spectral peaks. The consistency of the tracking measurement appears to be better for the 1 Hz oscillation, however more single tone experiments would be required to confirm whether this is due to the oscillation amplitude or frequency since in this case the target was moving at a significantly greater velocity.

3) QUANTITATIVE RESULTS

The identified qualitative trends are supported by the metric results. The time-domain correlation coefficients for these tests are high, ranging from 0.73 to 0.95, going from the lowest (Test 3) to the highest (Test 1) velocity cases, respectively. In the frequency domain, the values of the correlation coefficient range from 0.87 to 0.97, with better performance likewise associated with higher velocities (see Table 3). Despite the limited frequency resolution, Δf, due to the short acquisition duration, the dominant frequency peaks were accurately identified with absolute errors ranging from 0.009 Hz to 0.091 Hz, where these values are significantly less than Δf in all cases, indicating that the identified peaks are a match within measurement uncertainty. In terms of amplitude, the SAR measured velocities show a slight underestimation compared to the ground truth, where this discrepancy increases with decreasing target velocity. The RMSE confirms this trend – the relative RMSE increased consistently from 21.6% for Test 1 to 45.6% for Test 3. These findings all support the expectation that measurement accuracy decreases with decreasing target velocity.

B. AMPLITUDE MODULATION

1) PROCESSING PARAMETERS

The measurement results of the AM signals in Tests 4 to 7 are shown in Figures 12, 13, 14, and 15. The target velocities in these tests were significantly lower compared to the single frequency experiments, with $v_{r,\max}$ ranging from 1.42 $\mathrm{mm\,s^{-1}}$ to 5.25 $\mathrm{mm\,s^{-1}}$ (0.66 to 2.34 $\mathrm{mm\,s^{-1}}$ RMS) making them more representative of the vibrations expected for real structures. The RMS radial displacements recorded for these tests were very low, ranging from 0.10 mm to 0.23 mm. To compensate for the lower amplitudes and increased waveform complexity, it was found that the observation ratio η needed to be increased compared to the single frequency measurements to values ranging from 0.58 to 0.66, whilst the optimal overlap percentage Ω was more variable but remained within a similar range of 23% to 49%. This resulted in reduced sampling frequencies overall when comparing measurements of signals with the same carrier frequency; Test 1 compared with 6 and 7 indicates an approximate 40% drop in sampling frequency, and comparing Tests 2 and 3 with 4 and 5 shows an average decrease of approximately 25%. This led to a reduction in the maximum observable frequency, particularly in Tests 4 and 7, where the sampling frequency only marginally satisfied the Nyquist criterion of 4.4 and 2.4 Hz, respectively. Despite the reduction in f_s, t_sap was broadly similar to the single frequency measurements, except for Tests 6 and 7 involving the 1 Hz carrier which were significantly longer. For these measurements, the azimuth patch sizes were reduced to either 51 or 71 pixels, where this was due to the lower overall target velocity.

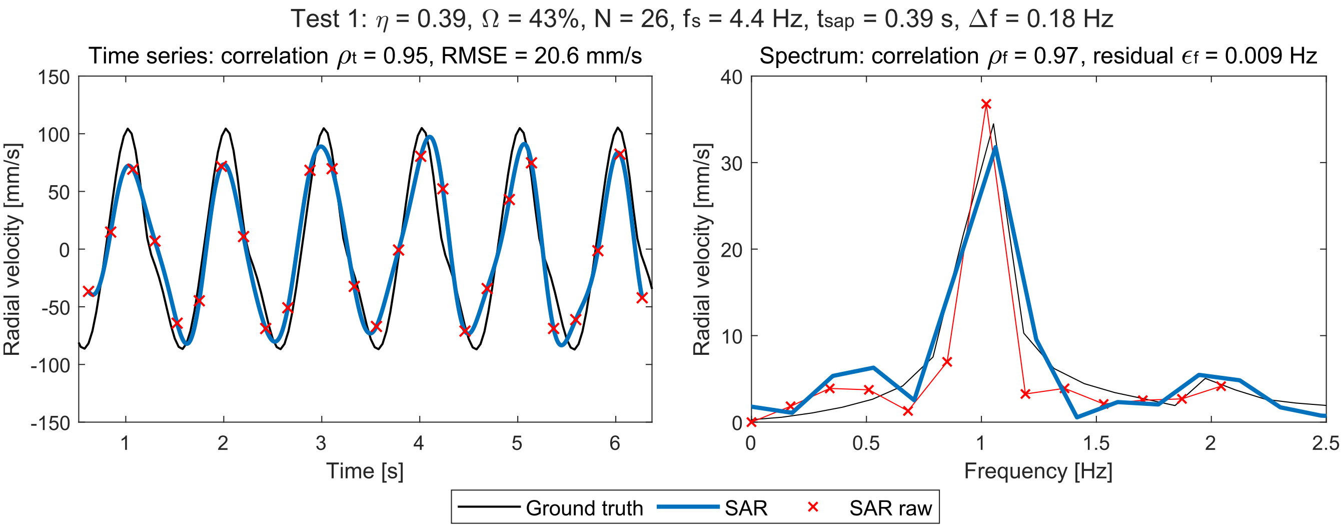

FIGURE 9. Time series and corresponding frequency spectrum from Test 1, with the shaker set to vibrate at 1 Hz with a peak radial velocity of $v_{r,\max} = 95.52\ \text{mms}^{-1}$ and an RMS of $v_{r,\text{RMS}} = 64.11\ \text{mms}^{-1}$. The plots compare the ground truth velocity (black line) with the SAR measurement: the raw output (red line with markers) and the sinc-interpolated result (blue line).

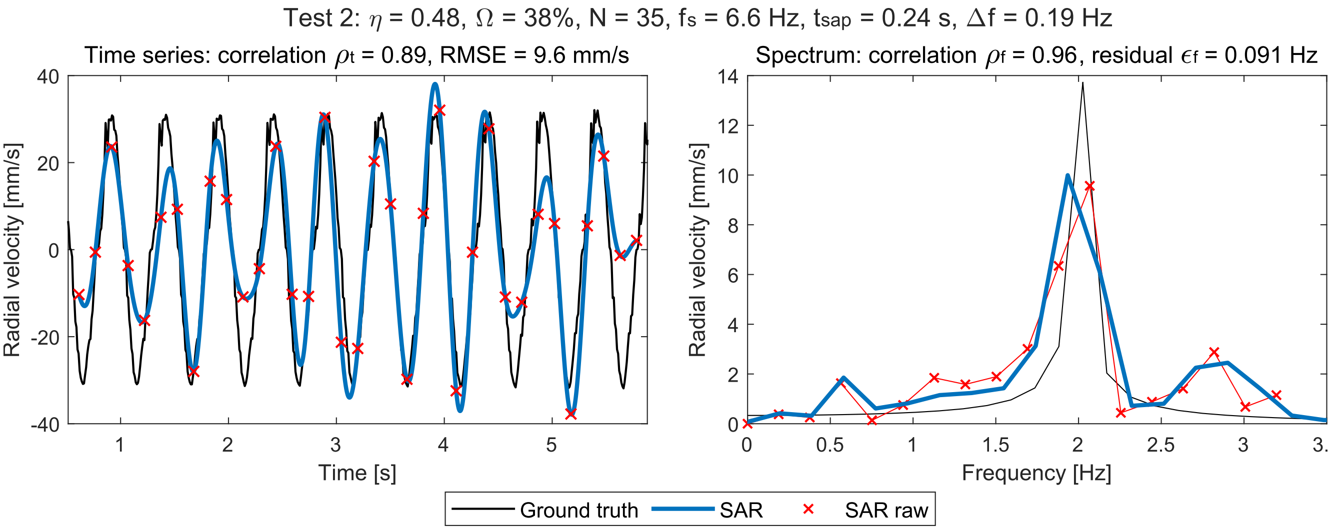

FIGURE 10. Time series and frequency spectrum results for Test 2, for a 2 Hz single frequency shaker motion with a $v_{r,\max} = 31.38\ \text{mms}^{-1}$ and $v_{r,\text{RMS}} = 20.70\ \text{mms}^{-1}$.

2) QUALITATIVE ANALYSIS

Compared to the higher velocity basic waveforms from Tests 1 to 3, a decrease in performance was observed for Tests 4 to 7. Despite this, the dominant frequency was accurately measured in all cases. Results from tests with a 2 Hz carrier (shown in Figures 12 and 13) were of generally lower quality. In Test 4, a secondary peak corresponding to the amplitude modulation was only marginally detectable, whilst in Test 5 both the modulation peaks were identified, although their amplitudes are comparable to the surrounding level of measurement uncertainty. Tests with a 1 Hz carrier (shown in Figures 14 and 15), showed clearer detections of the secondary peaks; in Test 7, these were more distinct compared to those in Test 6. The frequency match of the lower peak tended to be better than that of the higher peak, which was in general slightly underestimated. The relative amplitudes of the peaks were generally poorly estimated, but in all cases they remained lower than that of the carrier peak, which was accurately measured in Test 5, although it was generally underestimated in the other tests. Additionally, when detectable, the amplitude of the secondary peaks tended to be overestimated compared to the ground truth values.

3) QUANTITATIVE RESULTS

As shown in Table 3, the time-domain correlation coefficients for these tests range from 0.45 (Test 5) to 0.68 (Test 6), showing a decline compared to the single frequency

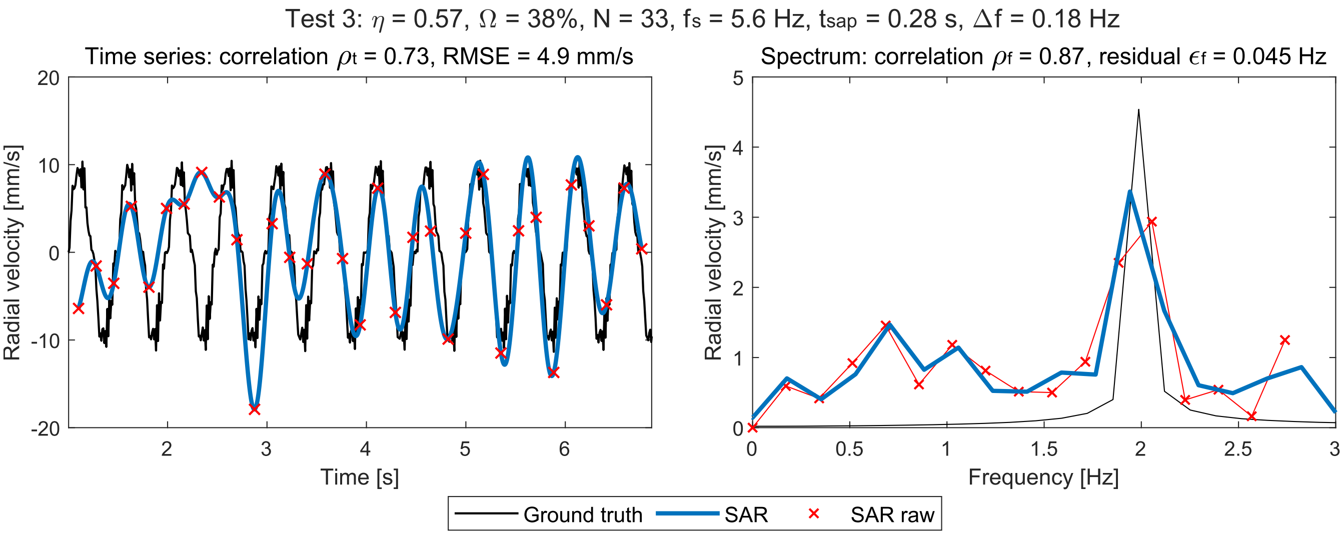

FIGURE 11. Time series and frequency spectrum results for Test 3, for a 2 Hz single frequency shaker motion with a $v_{r,\max} = 10.75$ mms^{-1} and $v_{r,\mathrm{RMS}} = 6.66$ mms^{-1}.

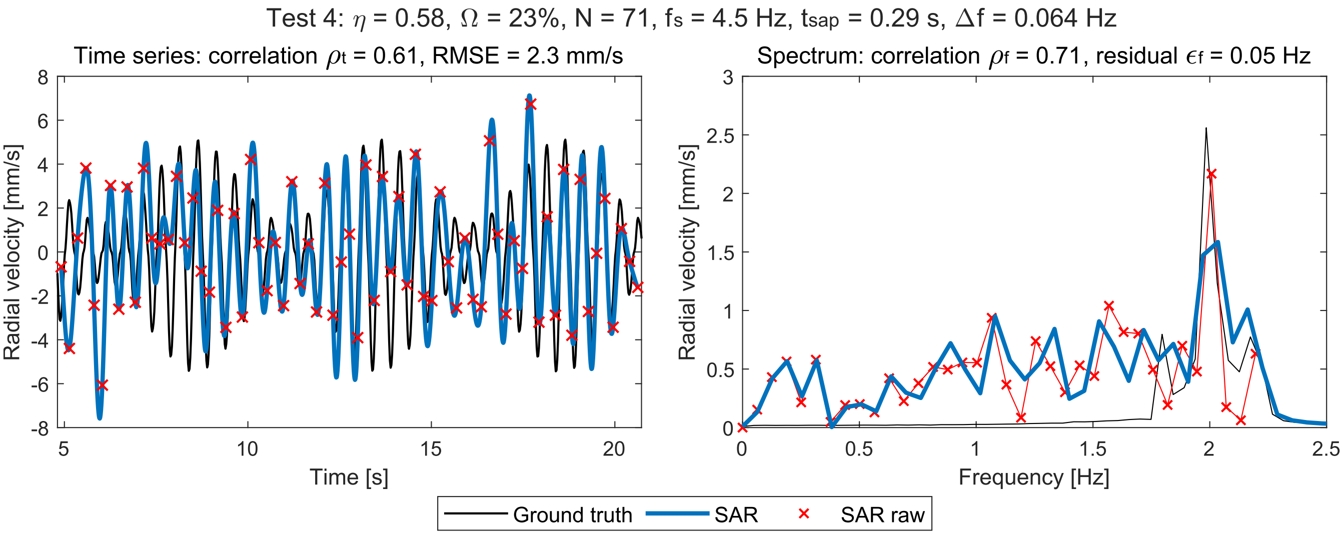

FIGURE 12. Time series and frequency spectrum results for Test 4, for a shaker motion governed by a 2 Hz carrier frequency with a 0.2 Hz amplitude modulation, with a $v_{r,\max} = 5.25$ mms^{-1} and $v_{r,\mathrm{RMS}} = 2.34$ mms^{-1}.

tests. Frequency-domain correlation values show a small variation from 0.70 (Test 7) to 0.75 (Test 6). The longer acquisition time of these tests resulted in an improved frequency spectrum resolution where $\Delta f \approx 0.07$ Hz. The frequency error, ϵ_f, for the dominant peak remained very good, ranging from 0.001 Hz to 0.050 Hz, and being consistently less than Δf. %RMSE values range from 38.3% (Test 6) to 68.5% (Test 5), with the error increasing as target velocity decreases for each carrier frequency, respectively.

Whilst Tests 5 and 6 had very similar target velocities, $v_{r,\mathrm{RMS}}$, of 1.31 mm s^{-1} and 1.46 mm s^{-1}, respectively, the measurement quality for Test 5 was significantly lower. This is indicated by the high RMSE and reduced time-domain correlation; the %RMSE for Test 5 reached 68.5%, compared to 38.3% for Test 6, and the time-domain correlation ρ_t was 0.45 versus 0.68. The frequency spectrum correlation, ρ_f, remained comparable however for the two tests, with only a slight decrease in Test 5 (0.73 versus 0.75). The decrease in performance can also be seen by visually comparing the measured signals in Fig. 13 and Fig. 14. These results suggest that the SPOT algorithm performs better measuring lower frequencies, and that the performance is not only dependent on the target velocity. Further support for this comes from Test 4, which featured a carrier frequency of 2 Hz and a higher velocity amplitude $v_{r,\mathrm{RMS}}$ of 2.34 than Test 6 (1 Hz carrier), but still resulted in a higher %RMSE of 43.8%.

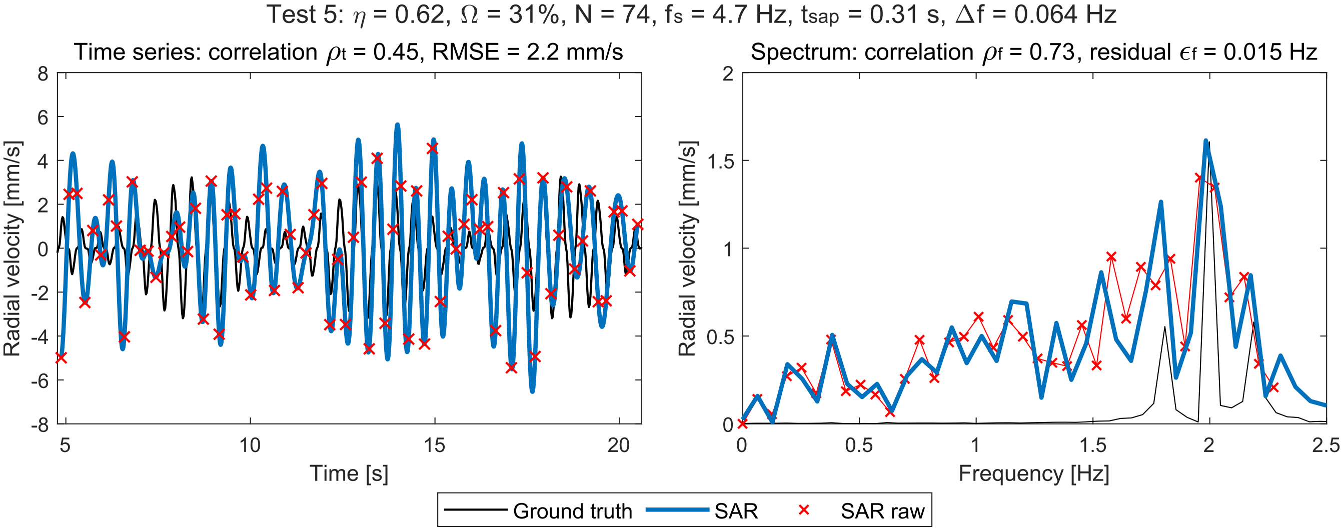

FIGURE 13. Time series and frequency spectrum results for Test 5, for a shaker motion governed by a 2 Hz carrier frequency with a 0.2 Hz amplitude modulation, with a $v_{r,\mathrm{max}} = 3.21$ mms^{-1} and $v_{r,\mathrm{RMS}} = 1.31$ mms^{-1}.

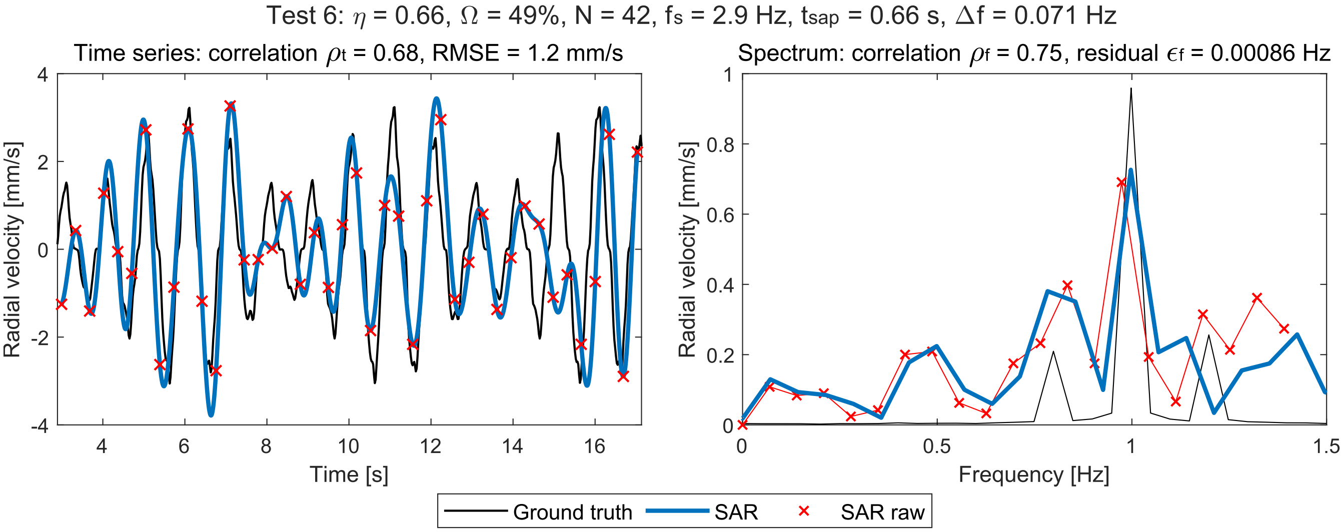

FIGURE 14. Time series and frequency spectrum results for Test 6, for a shaker motion governed by a 1 Hz carrier frequency with a 0.2 Hz amplitude modulation, with a $v_{r,\mathrm{max}} = 3.13$ mms^{-1} and $v_{r,\mathrm{RMS}} = 1.46$ mms^{-1}.

C. SUPERPOSITION AND LINEAR FREQUENCY MODULATION

1) PROCESSING PARAMETERS

Tests 8 and 9 (shown in Fig. 16 and 17) involved more complex target vibration signals, with additional frequency content and higher frequency components reaching up to 4 Hz. These tests also featured higher vibration velocities than those used for the AM motion experiments, more comparable to those for the single frequency tests. The peak radial velocity amplitudes $v_{r,\mathrm{max}}$ reached 21.99 mm s^{-1} for Test 8 and 58.04 mm s^{-1} for Test 9, with corresponding RMS values of 12.47 mm s^{-1} and 26.53 mm s^{-1}, respectively. The radial RMS displacements of these tests were $d_{r,\mathrm{RMS}} =$ 0.66 mm and 1.98 mm for Test 8 and 9, respectively. Due to the increased frequency content, higher sampling rates of 10.2 Hz and 10.5 Hz for Test 8 and 9, respectively, were necessary to guarantee the reconstruction of the full spectrum. The t_{sap} values of both tests were lower than the preceding measurements, being 0.17 and 0.15 s for Tests 8 and 9, respectively. The optimal azimuth patch sizes were once again found to approximately scale to the target velocity, where for Test 9 this was 131 pixels, the same as Test 1 where $v_{r,\mathrm{max}}$ was 95.52 mm s^{-1} and $v_{r,\mathrm{RMS}}$ was 64.11 mm s^{-1}.

2) QUALITATIVE ANALYSIS

In Test 8 (Fig. 16), the overall agreement of the SAR measured velocity with the ground truth in the time domain was relatively poor due to the presence of significant measurement uncertainty. This is also evident in the frequency-domain. Despite these limitations, the dominant frequencies

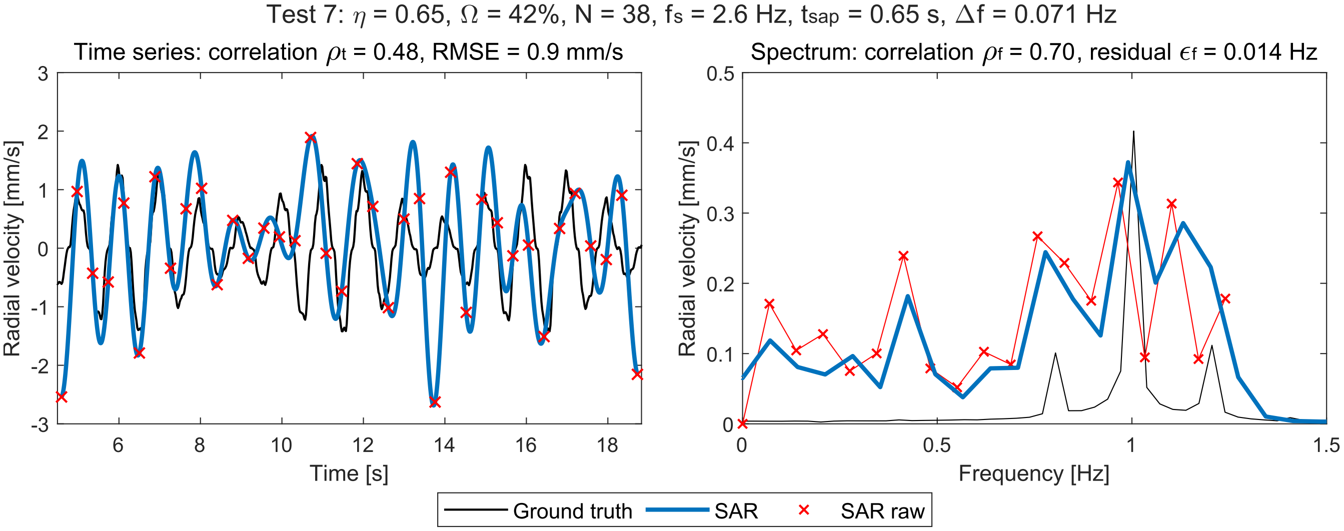

FIGURE 15. Time series and frequency spectrum results for Test 7, for a shaker motion governed by a 1 Hz carrier frequency with a 0.2 Hz amplitude modulation, with a $v_{r,\max} = 1.42\ \mathrm{mms}^{-1}$ and $v_{r,\mathrm{RMS}} = 0.66\ \mathrm{mms}^{-1}$.

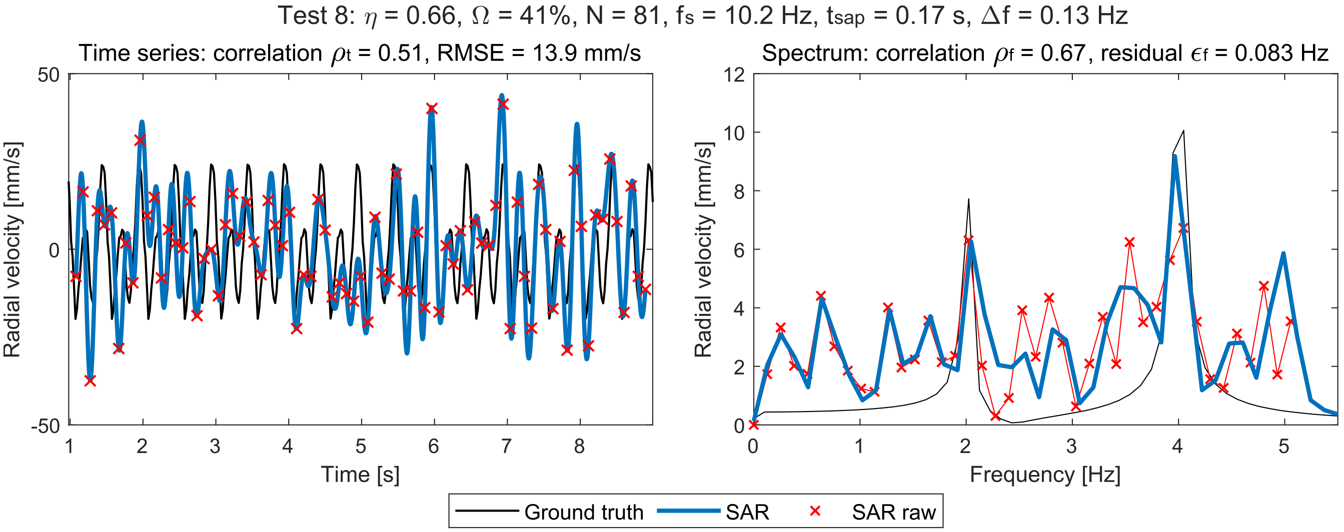

FIGURE 16. Time series and frequency spectrum results for Test 8, for a shaker motion of superposed 2 Hz and 4 Hz frequencies, with a $v_{r,\max} = 21.99\ \mathrm{mms}^{-1}$ and $v_{r,\mathrm{RMS}} = 12.47\ \mathrm{mms}^{-1}$.

of the two superposed signals of 2 Hz and 4 Hz are still correctly identified. A spurious third peak appears however at 5 Hz, reaching a magnitude comparable to the lower 2 Hz component. The amplitudes relative to the main frequency components were both well estimated, showing only slight underestimation relative to the ground truth.

The result for Test 9 shown in Fig. 17 showed significantly better performance in the time domain. The extracted signal closely resembled the ground truth, where the under- or overestimation of peak values was minor, although a bias towards underestimation was seen. The measurement improvement was likely due to the higher target velocity in Test 9 compared to the one in Test 8, despite the more complex signal content. In the frequency domain, all expected peaks up to 3.5 Hz were clearly identifiable. The relative amplitudes of these peaks also showed a good match, although the 1 Hz peak was nearly twice the amplitude of the ground truth, and the two most dominant components of 2.5 and 3 Hz were both underestimated. The ground truth peak at 4 Hz was not observed in the SAR data, possibly due to its relatively low amplitude compared to other components.

3) QUANTITATIVE RESULTS

Referring to Table 3, the time-domain correlation for Test 8 was 0.51, which is relatively low and aligns with the qualitative assessment. The spectrum correlation of 0.67 is slightly better, reflecting the correct identification of dominant frequency components. The frequency estimation error ϵ_f for the dominant 4 Hz peak was 0.083 Hz, which is below the spectral resolution $\Delta f = 0.13$ Hz and consistent with

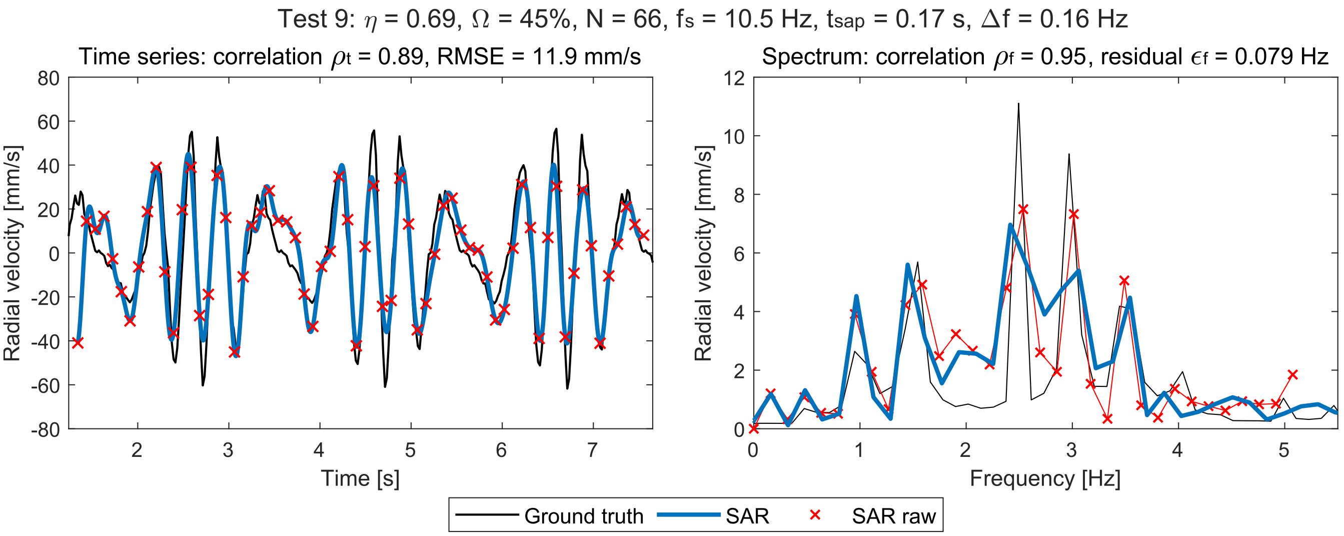

FIGURE 17. **Time series and frequency spectrum results for Test 9, for a shaker motion governed by a linear frequency sweep from 1 to 5 Hz, with a $v_{r,\max} = 58.04$ mms^{-1} and $v_{r,\mathrm{RMS}} = 26.53$ mms^{-1}.**

previous tests. The RMSE was 13.8 mm s^{-1}, corresponding to a high relative error of 63.2%.

In contrast, Test 9 yielded significantly better results, with a time-domain correlation of $\rho_t = 0.90$ and a frequency-domain correlation of $\rho_f = 0.95$. The frequency estimation error of $\epsilon_f = 0.074$ Hz was also less than the spectral resolution of $\Delta f = 0.16$ Hz, supporting the robustness of the frequency extraction. The RMSE was 11.5 mm s^{-1}, which corresponds to a relative error of 19.8%, highlighting the improved performance over Test 8.

VI. DISCUSSION

A. GENERAL MEASUREMENT PERFORMANCE

Several factors influence the LOS velocity measurement accuracy of the SPOT technique:

- oscillation amplitude of the velocity being measured,
- dominant frequency content of the vibration,
- signal complexity (e.g. sweep, superposition), and
- processing parameter selection (sampling, sub-aperture duration, overlap, etc.).

1) EFFECT OF OSCILLATION AMPLITUDE

Measurement error as defined by %RMSE increased as velocity amplitude decreased. For example, single-frequency tests (Tests 1-3) showed the %RMSE increasing from 21.6% to 45.6% for peak velocities decreasing from 95.5 mm s^{-1} to 10.75 mm s^{-1} (which in absolute terms was a decrease in RMSE from 20.6 mm s^{-1} to 4.9 mm s^{-1}, respectively); a similar trend was observed for AM signals. Effectively, this means the *velocity measurement uncertainty increases with decreasing amplitude*, which is the expected result. This behavior is visible in both the time domain and frequency domain of the velocities measured with MDSAR, where lower amplitude oscillations are associated with more spurious content and subsequently lower respective correlation values.

2) EFFECT OF DOMINANT FREQUENCY

For AM vibrations with velocities $v_{r,\mathrm{RMS}}$ between 0.66 and 2.34 mm s^{-1}, the carrier frequency of the vibration was shown to have a significant influence on the achievable performance of the measurement. A comparison between Test 5 and Test 6 illustrates this effect.

Test 5 featured a 2 Hz carrier and an RMS radial velocity of 1.31mm s^{-1}; its time and frequency-domain correlation coefficients were 0.45 and 0.73, corresponding to an RMSE of 68.5% of the peak value. In contrast, Test 6 employed a 1 Hz carrier with a comparable RMS radial velocity of 1.46 mm s^{-1}; here the time and frequency-domain correlations increased to 0.68 and 0.75, while the RMSE dropped to 38.3% of the peak value. A further comparison with Test 7 emphasises this conclusion; Test 7 had a carrier frequency of 1 Hz and a much lower RMS radial velocity of $v_{r,\mathrm{RMS}}0.66$ mm s^{-1}, resulting in time and frequency-domain correlation values of 0.48 and 0.70 and an RMSE of 64.1% of the peak value – and thus a measurement quality very similar to that of Test 5, where $v_{r,\mathrm{RMS}}$ was approximately double. These results demonstrate that for comparable vibration amplitudes, *lower dominant frequencies lead to more accurate measurements of the radial velocity*. Since these insights are strongly linked to the choice of optimal processing parameters, the influence of these parameters is further discussed later in Section VI-A4.

3) EFFECT OF SIGNAL COMPLEXITY

For more complex motion, such as the superposition and linear frequency sweep tests, the sensitivity of MDSAR to both velocity magnitude and frequency content was demonstrated further.

The superposition test (Test 8) was carried out with a relatively high $v_{r,\mathrm{RMS}}$ of 12.47 mm s^{-1}, however the achieved measurement quality was lower than for the simpler 1 Hz and 2 Hz cases analyzed previously. Test 8 resulted in time and frequency-domain correlation values of 0.51 and 0.67, respectively, and a %RMSE of 63.2%, whereas Test 4, with $v_{r,\mathrm{RMS}} = 2.34$ mm s^{-1}, achieved higher correlation values of 0.61 and 0.71, respectively, with a lower %RMSE of 45%.

In contrast, the linear frequency modulation test (Test 9) with a $v_{r,\mathrm{RMS}}$ of 26.53 mm s^{-1} yielded excellent results, with a temporal correlation of 0.89, spectral correlation of 0.95, and a %RMSE of 20.5% of the peak velocity. This relative RMSE value was the lowest of all the tests, which is notable given that Test 9 combined higher complexity and lower target velocity than Test 1. This insight suggests that other measurement variables, such as the observation geometry, likely have an impact on the results which has not been controlled for in these experiments.

4) PROCESSING PARAMETERS

A presentation of the full optimisation of the processing parameters, namely sub-aperture duration and overlap ratio, was outside the scope of this work. Nevertheless, the results presented revealed several phenomena resulting in the three points below, related to choosing appropriate processing parameters.

1) Nyquist sampling: the sampling frequency (f_s) must be above the Nyquist rate for the given waveform to be correctly sampled.
2) Azimuth cross-correlation precision: cross-correlation processing, and thus the pixel displacement measurement, is more accurate when the sub-aperture image has a finer azimuth resolution. A longer t_{sap} results in better azimuth resolution (see Eq. 1).
3) Motion-induced artifacts: longer sub-aperture times can make the feature less distinct and reduce tracking accuracy since the changing signal phase is integrated over a greater period. This imposes an upper bound on t_{sap}.

These effects compete, thus need to be optimised. Considering first effects 1 and 2, these are in opposition such that 1 favours shorter t_{sap} values for higher sampling rates whereas 2 favours the t_{sap} values which are as long as possible for greater azimuth precision. This conflict is resolved by allowing the overlap of sub-apertures, as increasing the overlap allows for a greater sampling frequency without reducing t_{sap}, therefore helping to satisfy both conditions simultaneously. Effect 3 then further constrains the overlap values allowed by effects 1 and 2 by its restriction on t_{sap}, and can be considered to be in opposition to effect 2. The combined result of all three effects is a moderate overlap value and an optimal f_s near the Nyquist rate. The upper bound on t_{sap} duration imposed by effect 3 increases for low frequency motion since the phase evolves more slowly, where in this case a higher azimuth resolution is then permitted, resulting in a higher quality measurement as the cross-correlation is more accurate. If t_{sap} is too long, the target motion initially becomes blurred in the sub-aperture image, and in the extreme case as t_{sap} approaches t_a the target becomes multiple or indistinct targets, as seen in the full aperture image (see Fig. 5).

The results of these effects are evident in Test 5 and 6, where carrier frequencies were 2 Hz and 1 Hz, respectively, and the RMS velocities were very similar. Both cases resulted in a sampling frequency near the Nyquist rate, whilst for the 1 Hz motion t_{sap} was approximately twice that of the 2 Hz case, which resulted in fewer sub-apertures. The resulting observation ratio (η) was similar for the two tests, indicating that t_{sap} scaled proportionally with the vibration period of the carrier. Due to the shorter t_{sap} required for the 2 Hz carrier motion, the azimuth resolution of each sub-aperture frame was reduced in comparison to that for 1 Hz. This resulted in slightly poorer results in terms of %RMSE and ρ_t (whilst ρ_f was about the same).

The sampling phenomena also explain the results for the more complex signals, for instance the high f_s for Test 8 and 9 of 10.2 Hz and 10.5 Hz, respectively. This is greater than expected compared to the AM signals, and is more similar to the single frequency tests. This is due to the greater target velocities which those two groups share, which increases azimuth displacements in the image. The tracking precision required is then reduced, allowing for higher sampling rates. This combination resulted in $t_{\mathrm{sap}} = 0.17$ s for each test, the lowest values recorded.

Regarding Test 8, the 2 Hz peak is lower proportionally than the 4 Hz peak possibly since the optimal parameters chosen by the metric would have been most sensitive to the match to the 4 Hz signal, and thus were likely not optimal for the measurement of the 2 Hz component, resulting in a bias. For Test 9, the amplitude discrepancies and the non-existent 4 Hz component were likely the result of the algorithm being optimised for compromise values to measure a range of frequencies concurrently, and the tracking precision was likely restricted by lower t_{sap} values resulting in less accurate estimations of the displacements. Additionally, since the 4 Hz component was of a low amplitude relative to the other frequencies, this would have had a lower weighting from the metric used to assess it. These findings suggest that improved results may be obtained by using multiple measurements on the same data which are optimised for small frequency ranges, and then synthesising these into one spectrum.

Apart from the sampling effects listed above, the tracking performance of cross-correlation is also closely related to the patch size (predominantly in the azimuth dimension). If the patch is too small, it will not be able to fully track the motion of a target since, in the extreme case, this will go beyond the bounds of the patch. If the patch is too large however, the tracking is more prone to confusion from noise or other bright targets in the image.

Whilst the optimum processing parameters were chosen for these results, in general a small range of values produced measurements approaching a similar quality. Given this and the difficulty in controlling all variables, some uncertainty in the conclusions about processing parameters remains.

B. FREQUENCY MEASUREMENT PERFORMANCE

The frequency measurement precision is fundamentally limited by the observation duration. In these experiments, the maximum SAR acquisition time was 16.01 s, giving a frequency resolution of roughly 0.064 Hz. This could limit distinguishing closely spaced modes in large civil structures. Longer effective acquisitions (up to $\sim$ 30 s in principle, system permitting [20], [21]) would proportionally refine the spectrum resolution. In the context of civil SHM, the frequency accuracy achievable with this technique cannot be smaller than the spectral resolution dictated by the observation time.

Despite these limitations, the dominant frequency was correctly measured in every test, including reliable (negligible error ϵ_f) measurements for AM signals with sub-millimetre radial displacements ranging from $d_{r,\mathrm{RMS}}$ from 0.23 to 0.10 mm. These results are the smallest confirmed displacements measured by this method and are a good indication of its potential suitability to SHM applications.

C. SUITABILITY FOR SHM

This section discusses the practical suitability of the SPOT MDSAR technique for VBSHM, particularly its potential to either substitute or complement conventional contact-based vibration monitoring. Using the presented results, this discussion focuses on whether SAR measurements can meet the typical requirements of SHM. It is reasonable to assume that the following findings extend only to large and slender structures such as long-span bridges or tall buildings, with expected LOS velocity values within the tested range, frequencies between 0.1 to 2.4 Hz, and exhibiting millimetre or sub-millimetre displacements. These assumptions however, will require future testing on real structures, which is outside the scope of this work.

Regarding the efficacy of MDSAR for VBSHM, it is essential to clarify that the required measurement accuracy depends on the monitoring objective. VBSHM generally aims to extract modal parameters such as natural frequencies, damping ratios, and mode-shapes; not to reconstruct the full time-history of structural vibrations. These parameters can be obtained using time-domain methods (e.g. stochastic subspace identification, SSI) or frequency-domain methods (e.g. frequency-domain decomposition, FDD), each with a different sensitivity to signal sampling, length, and noise. Time-domain methods require high temporal resolution and low-noise signals, which is difficult to satisfy with current SAR acquisition limitations. Frequency-domain methods, conversely, depend more on the spectral content and signal resolution, making them more suitable for MDSAR data.

The experimental results showed that radial RMS velocities as low as 3 $\mathrm{mm\,s^{-1}}$ could be measured with time-domain relative RMSE < 45%. Lower target velocities reduced the time-domain reconstruction accuracy, reaching an RMSE of 68.5% in the worst-case scenario. Notably, the dominant frequencies were consistently identified with frequency residuals below the spectral resolution, confirming the reliability of frequency measurement. This suggests that while MDSAR measurements may not yet be suitable for full time-history reconstructions or time-domain modal analyses, they are better-suited to frequency-domain SHM approaches, where the successful frequency measurement for a radial RMS velocity of 0.81 $\mathrm{mm\,s^{-1}}$ (radial RMS displacement of 0.10 mm) is an excellent indicator that MDSAR can be sensitive enough to measure SHM relevant motion.

Some practical considerations to note before applying this approach to real structures:

- Sampling frequency (f_s) and sub-aperture duration (t_sap) influence the sub-aperture azimuth resolution (see Section VI-A4). Lower aperture fractions improve f_s but degrade image resolution, hindering the tracking of the scatterers. Therefore, when low vibration frequencies are of interest, it is preferable to use longer sub-apertures to preserve a finer image resolution.
- The technique is inherently limited to measuring radial velocities, meaning that sensitivity depends on the satellite's viewing geometry. For vertical motion (e.g. bridges), near-nadir observations are ideal, while for horizontal motion (e.g. tall buildings), the orbit should be as tilted as possible for a high incidence angle.
- The high RMSE values of time-domain results prevent the precise extraction of mode-shapes and damping values but does not prevent the identification of dominant frequencies.
- The frequency resolution is limited by the achieved acquisition time, t_a. For structures with natural modes with a spacing more than that of the frequency resolution, the measured dominant frequency can serve as a key parameter for early-stage damage detection.

In conclusion, while SPOT MDSAR does not yet match the precision of conventional contact-based methods for full modal identification (specifically damping values and mode-shapes), it demonstrates strong potential for large-scale, remote measurement of dominant frequencies. This could support SHM frameworks where SAR data is paired with occasional on-site measurements to confirm or calibrate more detailed analyses.

D. FUTURE DEVELOPMENTS

The presented results demonstrate the capability of measuring vibration signatures comparable to those of real infrastructure from spaceborne SAR imagery, establishing a well-validated foundation for future work. Given the limitations of the presented technique for vibration measurements, there are several strategies that could be employed to improve the performance and practicality of MDSAR for VBSHM:

- *Algorithm improvements*: the SPOT algorithm, as an image-domain method, requires patch-size optimisation and is inherently limited by image resolution. Future research could explore phase-domain methods, which may offer greater sensitivity for micro-motion measurement, and issues arising from effect 3 in Section VI-A4 may be alleviated. Moreover, signal enhancement techniques such as singular value decomposition (SVD) or Bayesian filtering could help mitigate noise and increase robustness.

- *Integration of knowledge of structural dynamics*: integrating structural models (e.g. simplified dynamic equations or finite element models), or simply imposing physical constraints into the velocity reconstruction workflow, may allow for better fitting of measured data.
- *Orbit planning and acquisition strategies*: since MDSAR is only sensitive to the radial component of motion, observation geometry plays an important role. Future satellite tasking could prioritize near-nadir acquisitions for vertical motion measurements, or steep incidence angles for horizontal displacements. Likewise, longer-duration acquisitions would enhance spectral resolution and improve the detection of closely spaced frequency modes.
- *Combination of multiple passes*: combining measurements from different passes or viewing geometries may enable the reconstruction of full three-dimensional motion. Furthermore, these could increase redundancy and improve confidence in frequency detection.

VII. CONCLUSION

This work investigated the metrological effectiveness of MDSAR for measuring target vibrations from single-pass SAR images, focusing on vibrational signals relevant to SHM of infrastructure. The SPOT algorithm was used as a representative method among various potential techniques.

To assess the performance and limitations of MDSAR, a comprehensive experimental campaign was conducted using an isolated shaker target under controlled conditions. A wide range of vibration types were generated, including single frequency sinusoids, AM signals, a frequency superposition and a linear frequency modulation. Peak radial velocities varied from high amplitudes ($95.52\ \mathrm{mm\,s^{-1}}$, 13.96 mm radial displacement) to very low amplitudes ($1.42\ \mathrm{mm\,s^{-1}}$, radial displacement of 0.19 mm), reflecting SHM relevant ranges.

MDSAR measured the time-history of LOS velocity, with RMSE errors of $20.6\ \mathrm{mm\,s^{-1}}$ (21.6% of ground truth peak value) and $0.9\ \mathrm{mm\,s^{-1}}$ (63.2%), for the highest ($95.52\ \mathrm{mm\,s^{-1}}$, single frequency) and lowest ($1.42\ \mathrm{mm\,s^{-1}}$, AM) amplitudes, respectively. Percentage RMSE increased in relative terms as the velocity amplitude decreased and the signal complexity increased. Signals dominated by lower frequencies produced better results than those with higher-frequency content.

The dominant frequency was correctly identified in all test cases, down to RMS radial displacements of 0.10 mm for two AM signals with RMS radial velocities of 1.31 and $0.66\ \mathrm{mm\,s^{-1}}$. Frequency peak residuals consistently fell below the spectral resolution limit. The SAR acquisition duration (longest recorded $\sim$ 16 s) constrains frequency resolution ($\sim$ 0.064 Hz), which may not be sufficient for distinguishing closely spaced structural modes in civil SHM, although longer acquisitions of $\sim$ 30 s are feasible. Spectral correlation values (ρ_f) were consistently higher than the temporal correlation values (ρ_t), indicating that the technique is better at reconstructing the frequency content of the signal, rather than the full time-history of the radial velocity.

Overall, this work demonstrated that information relevant for VBSHM can be measured from SAR data, even with a relatively simple approach like the SPOT technique. The achievable level of accuracy – compared to synchronous ground truth time series data – indicated that whilst limitations remain in reconstructing full time-histories, dominant vibrational frequencies were measured effectively, even for very small displacements similar to those expected from infrastructure. These results show strong metrological evidence that MDSAR can be used for spectral SHM applications, with significant potential for continuing improvements.

Future developments include improving the accuracy and robustness of the SPOT method by incorporating knowledge of structural dynamics, exploring the choice for the optimal extraction parameters and patch size selection, extending the validation to a case study of a real bridge, and finally the use of other MDSAR techniques – for instance those which exploit the phase content of SAR data.

ACKNOWLEDGMENT

The authors would like to acknowledge the collaboration of Umbra Space in providing SAR images, and the University of Strathclyde and the University of Trento for helping conduct the experiments of the study, with particular thanks to Daniel Tonelli and Matteo Turrini. They would also like to thank Ernesto Imbembo, Marc Zimmermanns, and Maria Michela Corvino for their support throughout this research.

REFERENCES

[1] J. J. Moughty and J. R. Casas, "A state of the art review of modal-based damage detection in bridges: Development, challenges, and solutions," *Appl. Sci.*, vol. 7, no. 5, p. 510, May 2017, doi: 10.3390/app7050510.

[2] W. Fan and P. Qiao, "Vibration-based damage identification methods: A review and comparative study," *Struct. Health Monitor.*, vol. 10, no. 1, pp. 83–111, Jan. 2011, doi: 10.1177/1475921710365419.

[3] Z. Sun, M. Mahmoodian, A. Sidiq, S. Jayasinghe, F. Shahrivar, and S. Setunge, "Optimal sensor placement for structural health monitoring: A comprehensive review," *J. Sensor Actuator Netw.*, vol. 14, no. 2, p. 22, Feb. 2025, doi: 10.3390/jsan14020022.

[4] J. M. W. Brownjohn, "Structural health monitoring of civil infrastructure," *Philos. Trans. Roy. Soc. A, Math., Phys. Eng. Sci.*, vol. 365, no. 1851, pp. 589–622, Feb. 2007, doi: 10.1098/rsta.2006.1925.

[5] L. Ngeljaratan and M. A. Moustafa, "Structural health monitoring and seismic response assessment of bridge structures using target-tracking digital image correlation," *Eng. Struct.*, vol. 213, Jun. 2020, Art. no. 110551, doi: 10.1016/j.engstruct.2020.110551.

[6] S. Jiang, J. Zhang, and C. Gao, "Bridge deformation measurement using unmanned aerial dual camera and learning-based tracking method," in *Structural Control and Health Monitoring*, Y.-J. Cha, Ed., Hoboken, NJ, USA: Wiley, Apr. 2023, pp. 1–19, doi: 10.1155/2023/4752072.

[7] E. Kaartinen, K. Dunphy, and A. Sadhu, "LiDAR-based structural health monitoring: Applications in civil infrastructure systems," *Sensors*, vol. 22, no. 12, p. 4610, Jun. 2022, doi: 10.3390/s22124610.

[8] A. Trias-Blanco, J. Gong, and F. Moon, "Characterization of operational vibrations of steel-girder highway bridges via LiDAR," *Remote Sens.*, vol. 15, no. 4, p. 1003, Feb. 2023, doi: 10.3390/rs15041003.

[9] T. Panigati, M. Zini, D. Striccoli, P. F. Giordano, D. Tonelli, M. P. Limongelli, and D. Zonta, "Drone-based bridge inspections: Current practices and future directions," *Autom. Construct.*, vol. 173, May 2025, Art. no. 106101, doi: 10.1016/j.autcon.2025.106101.

[10] C. Gentile and G. Bernardini, "An interferometric radar for non-contact measurement of deflections on civil engineering structures: Laboratory and full-scale tests," *Struct. Infrastruct. Eng.*, vol. 6, no. 5, pp. 521–534, Oct. 2010, doi: 10.1080/15732470903068557.

[11] C. Michel and S. Keller, "Advancing ground-based radar processing for bridge infrastructure monitoring," *Sensors*, vol. 21, no. 6, p. 2172, Mar. 2021, doi: 10.3390/s21062172.

[12] M. Sofi, E. Lumantarna, P. A. Mendis, C. Duffield, and A. Rajabifard, "Assessment of a pedestrian bridge dynamics using interferometric radar system IBIS-FS," *Proc. Eng.*, vol. 188, pp. 33–40, Jan. 2017, doi: 10.1016/j.proeng.2017.04.454.

[13] J. Xi, Z. Suo, and J. Ti, "The first experimental validation of a communication base station as a ground-based SAR for deformation monitoring," *Remote Sens.*, vol. 17, no. 7, p. 1129, Mar. 2025, doi: 10.3390/rs17071129.

[14] D. Cusson, C. Rossi, and I. F. Ozkan, "Early warning system for the detection of unexpected bridge displacements from radar satellite data," *J. Civil Struct. Health Monitor.*, vol. 11, no. 1, pp. 189–204, Feb. 2021, doi: 10.1007/s13349-020-00446-9.

[15] P. Milillo, G. Giardina, D. Perissin, G. Milillo, A. Coletta, and C. Terranova, "Pre-collapse space geodetic observations of critical infrastructure: The morandi bridge, Genoa, Italy," *Remote Sens.*, vol. 11, no. 12, p. 1403, Jun. 2019, doi: 10.3390/rs11121403.

[16] X. Qin, M. Liao, M. Yang, and L. Zhang, "Monitoring structure health of urban bridges with advanced multi-temporal InSAR analysis," *Ann. GIS*, vol. 23, no. 4, pp. 293–302, Oct. 2017, doi: 10.1080/19475683.2017.1382572.

[17] D. Tonelli, V. F. Caspani, A. Valentini, A. Rocca, R. Torboli, A. Vitti, D. Perissin, and D. Zonta, "Interpretation of bridge health monitoring data from satellite InSAR technology," *Remote Sens.*, vol. 15, no. 21, p. 5242, Nov. 2023, doi: 10.3390/rs15215242.

[18] D. Tonelli, A. Valentini, A. Rocca, S. Zorzi, A. Lotti, and D. Zonta, "Uncertainty quantification of satellite InSAR-monitoring of bridges: A case study," *Ce/Papers*, vol. 6, no. 5, pp. 900–906, Sep. 2023, doi: 10.1002/cepa.1991.

[19] V. C. Chen, *The Micro-Doppler Effect in Radar*, 2nd ed. Norwood, MA, USA: Artech House, 2019.

[20] (2023). *Delivering Global Omniscience • Umbra Space*. [Online]. Available: https://umbra.space/

[21] *Capella Space X-Band Synthetic Aperture Radar*. Accessed: Jan. 9, 2026. [Online]. Available: https://www.eoportal.org/satellite-missions/capella-x-sar

[22] *Single Look Complex Image—ICEYE Product Documentation*. Accessed: Jan. 9, 2026. [Online]. Available: https://sar.iceye.com/5.0/productFormats/slc/

[23] C. Clemente, D. Tonelli, A. Lotti, F. Rollo, C. Ilioudis, S. D. Riofrio, F. Biondi, E. Tubaldi, M. Macdonald, D. Zonta, M. Zavagli, M. Costantini, F. Minati, F. Vecchioli, P. Milillo, M. Zimmermanns, E. Imbembo, and M. M. Corvino, "On micro-motion extraction from high resolution X-band SAR products," in *Proc. IEEE Int. Geosci. Remote Sens. Symp.*, Athens, Greece, Jul. 2024, pp. 1182–1186, doi: 10.1109/IGARSS53475.2024.10642825.

[24] F. Rollo, C. Ilioudis, G. Zefi, A. Lotti, D. Tonelli, M. Zavagli, M. Constantini, D. Zonta, E. Tubaldi, P. Milillo, M. Macdonald, and C. Clemente, "Micro-motion extraction from spotlight SAR using a modified backprojection approach," in *Microwave Remote Sensing: Data Processing and Applications III*, E. Santi, F. Bovenga, C. Notarnicola, and N. Pierdicca, Eds., Bellingham, WA, USA: SPIE, Nov. 2024, p. 12, doi: 10.1117/12.3031678.

[25] M. Soumekh, *Synthetic Aperture Radar Signal Processing With MATLAB Algorithms*. Hoboken, NJ, USA: Wiley, 1999.

[26] *Sensor Independent Complex Data (SICD)*, vol. 1, Design & Implementation Description Document NGA.STND.0024-1_1.2.1, Dec. 2018. [Online]. Available: https://nsgreg.nga.mil/doc/view?i=4900

[27] M. Ruegg, E. Meier, and D. Nuesch, "Vibration and rotation in millimeter-wave SAR," *IEEE Trans. Geosci. Remote Sens.*, vol. 45, no. 2, pp. 293–304, Feb. 2007, doi: 10.1109/TGRS.2006.887025.

[28] F. Rollo, C. Ilioudis, and C. Clemente, "Advances in micro-Doppler processing in synthetic aperture radar: A review of techniques, results, and future trends," *IEEE Geosci. Remote Sens. Mag.*, vol. 13, no. 4, pp. 243–265, Dec. 2025, doi: 10.1109/MGRS.2025.3573099.

[29] R. Raney, "Synthetic aperture imaging radar and moving targets," *IEEE Trans. Aerosp. Electron. Syst.*, vol. AES-7, no. 3, pp. 499–505, May 1971, doi: 10.1109/TAES.1971.310292.

[30] V. C. Chen, F. Li, S.-S. Ho, and H. Wechsler, "Micro-Doppler effect in radar: Phenomenon, model, and simulation study," *IEEE Trans. Aerosp. Electron. Syst.*, vol. 42, no. 1, pp. 2–21, Jan. 2006, doi: 10.1109/TAES.2006.1603402.

[31] A. B. Vattulainen, F. Rollo, A. Lotti, D. Tonelli, S. D. Riofrio, E. Tubaldi, D. Zonta, C. Ilioudis, P. Milillo, and C. Clemente, "Bridge vibration measurements from very high-resolution spaceborne SAR," in *Proc. IEEE SENSORS*, Oct. 2024, pp. 1–4, doi: 10.1109/SENSORS60989.2024.10785004.

[32] Q. Wang, M. Pepin, R. J. Beach, R. Dunkel, T. Atwood, B. Santhanam, W. Gerstle, A. W. Doerry, and M. M. Hayat, "SAR-based vibration estimation using the discrete fractional Fourier transform," *IEEE Trans. Geosci. Remote Sens.*, vol. 50, no. 10, pp. 4145–4156, Oct. 2012, doi: 10.1109/TGRS.2012.2187665.

[33] Q. Wang, M. Pepin, A. Wright, R. Dunkel, T. Atwood, B. Santhanam, W. Gerstle, A. W. Doerry, and M. M. Hayat, "Reduction of vibration-induced artifacts in synthetic aperture radar imagery," *IEEE Trans. Geosci. Remote Sens.*, vol. 52, no. 6, pp. 3063–3073, Jun. 2014, doi: 10.1109/TGRS.2013.2269138.

[34] A. Anghel, G. Vasile, C. Ioana, R. Cacoveanu, and S. Ciochina, "Micro-Doppler reconstruction in spaceborne SAR images using azimuth time–frequency tracking of the phase history," *IEEE Geosci. Remote Sens. Lett.*, vol. 13, no. 4, pp. 604–608, Apr. 2016, doi: 10.1109/LGRS.2016.2530817.

[35] A. Focsa, A. Anghel, G. Nico, I. Maggio, M. Datcu, and M. Corvino, "Vibration-induced micro-Doppler estimation in spaceborne SAR images using Doppler centroid tracking across Azimuth sub-apertures," in *Proc. IEEE Int. Radar Conf. (RADAR)*, May 2025, pp. 1–6, doi: 10.1109/radar52380.2025.11031947.

[36] I. Djurović and L. Stanković, "Quasi-maximum-likelihood estimator of polynomial phase signals," *IET Signal Process.*, vol. 8, no. 4, pp. 347–359, Jun. 2014, doi: 10.1049/iet-spr.2013.0104.

[37] F. Biondi, P. Addabbo, S. L. Ullo, C. Clemente, and D. Orlando, "Perspectives on the structural health monitoring of bridges by synthetic aperture radar," *Remote Sens.*, vol. 12, no. 23, p. 3852, Nov. 2020, doi: 10.3390/rs12233852.

[38] F. Biondi, P. Addabbo, C. Clemente, S. L. Ullo, and D. Orlando, "Monitoring of critical infrastructures by micromotion estimation: The Mosul Dam destabilization," *IEEE J. Sel. Topics Appl. Earth Observ. Remote Sens.*, vol. 13, pp. 6337–6351, 2020, doi: 10.1109/JSTARS.2020.3030977.

[39] P. Milillo, R. Bürgmann, P. Lundgren, J. Salzer, D. Perissin, E. Fielding, F. Biondi, and G. Milillo, "Space geodetic monitoring of engineered structures: The ongoing destabilization of the Mosul Dam, Iraq," *Sci. Rep.*, vol. 6, no. 1, p. 37, Dec. 2016, doi: 10.1038/srep37408.

[40] C. E. Shannon, "Communication in the presence of noise," *Proc. IRE*, vol. 37, no. 1, pp. 10–21, Jan. 1949, doi: 10.1109/JRPROC.1949.232969.

[41] *SatNOGS DB—Umbra 02*. Accessed: Jan. 9, 2026. [Online]. Available: https://db.satnogs.org/satellite/TPDX-4064-2548-6167-6896

[42] *APS 113-AB—SPEKTRA*. Accessed: Jan. 9, 2026. [Online]. Available: https://www.spektradresden.com/en/product/details/calibration-solutions,device-testing/erreger-und-komponenten,kalibriererreger-und-komponenten/schwingung/aps-113-ab.html

[43] S. D. Robertson, "Targets for microwave radar navigation," *Bell Syst. Tech. J.*, vol. 26, no. 4, pp. 852–869, Oct. 1947, doi: 10.1002/j.1538-7305.1947.tb01325.x.

[44] *Inertial-Vibration Test System: TIRA GmbH*. Accessed: Jan. 9, 2026. [Online]. Available: https://www.tira-gmbh.de/en/vibration-test-systems/vibration-testsystems/inertial-vibration-test-system/

[45] *APS 400—APS Dynamics*. Accessed: Jan. 9, 2026. [Online]. Available: https://www.apsdynamics.com/en/products/details/vibration-exciter/aps-400.html

ALEKSANTERI B. VATTULAINEN (Member, IEEE) received the M.Phys. degree (Hons.) in physics from the University of St Andrews, U.K., in 2019, the M.S.E.C.E. degree in electrical and computer engineering from Georgia Institute of Technology, GA, USA, in 2020, and the Ph.D. degree in millimetre-wave radar engineering from the University of St Andrews, in 2024. Since 2024, he has been a Research Associate with the Sensor Signal Processing and Security Laboratory as part of the Centre for Signal and Image Processing with the University of Strathclyde, U.K. His research interests include micro-Doppler analysis and SAR signal processing, radar sea clutter measurement, and millimetre-wave, and sub-THz radar system design.

ALESSANDRO LOTTI received the Laurea (B.Sc.) and Laurea Specialistica (M.Sc.) degrees from the University of Trento, Italy, in 2019 and 2022, respectively, where he is currently pursuing the Ph.D. degree in civil engineering. He spent a year as a sponsored Visiting Researcher with the University of Strathclyde, U.K., in 2024, where he collaborated with the Civil and Environmental Engineering Department and the Sensor Signal Processing and Security Laboratories. His research focuses on structural health monitoring and remote sensing, with a particular emphasis on the use of SAR for long-term displacement analysis and vibration-based monitoring.

SEBASTIÁN DÍAZ RIOFRÍO was born in San Sebastián, Spain, in 1995. He received the B.Sc. degree in telecommunications systems and the M.Sc. degree in telecommunications engineering from the Tecnun School of Engineering, University of Navarra, San Sebastián, in 2017 and 2019, respectively, and the Ph.D. degree in electrical and electronic engineering from the University of Strathclyde, Glasgow, U.K., in 2025. His field of study is signal processing with a focus on radar. He was a Research Assistant with the University of Strathclyde on multiple projects, including Artificial Intelligence for Space Surveillance and Tracking (AI4SST), the Intercontinental Radar Bistatic System (IRIS), Bridge Monitoring Based on Single-Pass SAR Images, and River Flow Monitoring via Single-Look Complex SAR Images. He has worked on radar system design, SAR image processing, and the development of both conventional, and AI-driven signal processing methods. He also completed internships at Tecnalia Research and Innovation and CEIT, Spain, focusing on signal processing and antenna design. His publications include "Performance Analysis of Ground-Based Long Baseline Radar Distributed Systems for Space Situational Awareness" (*IET Radar, Sonar and Navigation*, in 2023). His research interests include radar signal processing, image processing, machine learning, and radar systems for space situational awareness. He was a recipient of the Wiley Top Viewed Article Award, in 2024, and the Connecting Talent scholarship from Fomento San Sebastián, in 2019.

CHIARA SUPPI (Graduate Student Member, IEEE) received the M.S. degree in civil engineering from the University of Trento, Trento, Italy, in 2023, where she is currently pursuing a Ph.D. degree, with a focus on vibration-based structural health monitoring using a single SAR image.

ENRICO TUBALDI is currently a Reader in structural engineering with the Department of Civil and Environmental Engineering and the Centre for Intelligent Infrastructure, University of Strathclyde, U.K., which he joined as a Lecturer, in October 2017. Previously, he was a Marie Curie Research Fellow with Imperial College London. His research focuses on risk assessment and monitoring of structures and infrastructure assets under natural hazards, such as earthquakes and floods, and on computational structural mechanics. He has authored more than 85 refereed articles in these areas.

DANIELE ZONTA received the M.Sc. degree in civil engineering from the University of Padua, Italy, in 1996, and the Ph.D. degree in structural mechanics from the University of Bologna, Italy, in 2000. He is currently a Professor of structural engineering with the University of Trento, Italy, with courtesy appointments at the University of Strathclyde, U.K., and the Institute for Photonics and Nanotechnologies, CNR. He has been a Visiting Scholar with UC San Diego, Princeton, USA, and the University of Michigan, USA. He is author of over 160 publications, he was named SHM Person of the Year in 2014 by the SAGE SHM editorial board. His research focuses on infrastructure management, structural health monitoring, sensing technologies, and decision-making for civil infrastructure. He is a Council Member of ISHMII, a Senior Member of SPIE, a Board Member of IASCM, a Chair of fib TG3.5 (Forensic Engineering), and the Founder of the International Summer School on Smart Materials and Structures. He is the Co-Founded Intelligent Infrastructure Innovation, a University of Trento startup.

PIETRO MILILLO (Senior Member, IEEE) received the bachelor's degree (Laurea) and the master's degree in physics from the University of Bari, Bari, Italy, in 2012, with a thesis on synthetic aperture radar and GPS data processing, and the Ph.D. degree in environmental engineering from the University of Basilicata, Potenza, Italy, in 2016, with a thesis on the synergistic use of synthetic aperture radar (SAR) constellations for studying natural and anthropogenic phenomena Over the years, he has held various positions, including NASA Postdoctoral Program (NPP) Fellow with JPL, the Scientist in radar science and engineering with JPL, and an Associate Project Scientist in Earth system science with the University of California, Irvine, Irvine, CA, USA. Since 2021, he has been an Assistant Professor in geosensing system engineering with the Department of Civil and Environmental Engineering, University of Houston, Houston, TX, USA. He is currently a Guest Scientist with German Aerospace Center (DLR), Munich, Germany. He has authored or co-authored more than 50 research articles in leading international journals. His research focuses on the synergistic use of remote sensing data exploitation and innovative approaches for computational analyses in Earth and cryosphere science and natural/anthropogenic hazard response. He is particularly interested in analyzing how the new generation of remote sensing instruments leads to a more effective, near real-time disaster monitoring, assessment, and response. His multidisciplinary research interests include Earth science, cryosphere, and disaster response.

CARMINE CLEMENTE (Senior Member, IEEE) received the Laurea (B.Sc.) and Laurea Specialistica (M.Sc.) degrees (cum laude) in telecommunications engineering from the Università degli Studi del Sannio, Benevento, Italy, in 2006 and 2009, respectively, and the Ph.D. degree in electronic and electrical engineering from the University of Strathclyde, Glasgow, U.K., in 2012. He is currently a Professor with the Department of Electronic and Electrical Engineering, University of Strathclyde, working on advanced radar signal processing algorithms, micro-doppler analysis, SAR image processing, and advanced radar applications. He directs the Centre for Signal and Image Processing and the Sensor Signal Processing and Security Laboratories, University of Strathclyde, where his group's research interests include micro-Doppler signature analysis and extraction, waveform design, passive and multistatic radars, automatic target recognition, electronic surveillance, space situation awareness, ballistic missile defense, automotive radars, applications of radars in industry 4.0, and agritech and statistical signal processing. He is the Chair of the Advanced Signal Processing Focus Group of the Electromagnetic Sensing Interest Group–The U.K. Radar Society. He is an Associate Editor of IEEE TRANSACTIONS ON AEROSPACE AND ELECTRONIC SYSTEMS.

• • •